

Crystalline all-inorganic lead-free $\text{Cs}_3\text{Sb}_2\text{I}_9$ perovskite microplates with ultra-fast photoconductive response and robust thermal stability

Sujit Kumer Shil^{1,3,§}, Fei Wang^{2,4,5,§} (✉), Zhengxun Lai², You Meng², Yunpeng Wang⁴, Dongxu Zhao⁴, Mohammad Kamal Hossain^{1,6}, Kingsley O. Egbo¹, Ying Wang¹, Kin Man Yu¹ (✉), and Johnny C. Ho^{2,5} (✉)

Nano Res., **Just Accepted Manuscript** • <https://doi.org/10.1007/s12274-021-3351-x>
<http://www.thenanoresearch.com> on Jan. 21, 2021

© Tsinghua University Press 2021

Just Accepted

This is a “Just Accepted” manuscript, which has been examined by the peer-review process and has been accepted for publication. A “Just Accepted” manuscript is published online shortly after its acceptance, which is prior to technical editing and formatting and author proofing. Tsinghua University Press (TUP) provides “Just Accepted” as an optional and free service which allows authors to make their results available to the research community as soon as possible after acceptance. After a manuscript has been technically edited and formatted, it will be removed from the “Just Accepted” Web site and published as an ASAP article. Please note that technical editing may introduce minor changes to the manuscript text and/or graphics which may affect the content, and all legal disclaimers that apply to the journal pertain. In no event shall TUP be held responsible for errors or consequences arising from the use of any information contained in these “Just Accepted” manuscripts. To cite this manuscript please use its Digital Object Identifier (DOI®), which is identical for all formats of publication.

TABLE OF CONTENTS (TOC)

Crystalline All-Inorganic Lead-Free $\text{Cs}_3\text{Sb}_2\text{I}_9$ Perovskite Microplates with Ultra-Fast Photoconductive Response and Robust Thermal Stability

Sujit Kumer Shil,^{1,3} Fei Wang,^{*,2,4,5} Zhengxun Lai,² You Meng,² Yunpeng Wang,⁴ Dongxu Zhao,⁴ Mohammad Kamal Hossain,^{1,6} Kingsley O. Egbo,¹ Ying Wang,¹ Kin Man Yu,^{*,1} and Johnny C. Ho^{*,2,5}

¹ Department of Physics, City University of Hong Kong, Kowloon, Hong Kong SAR

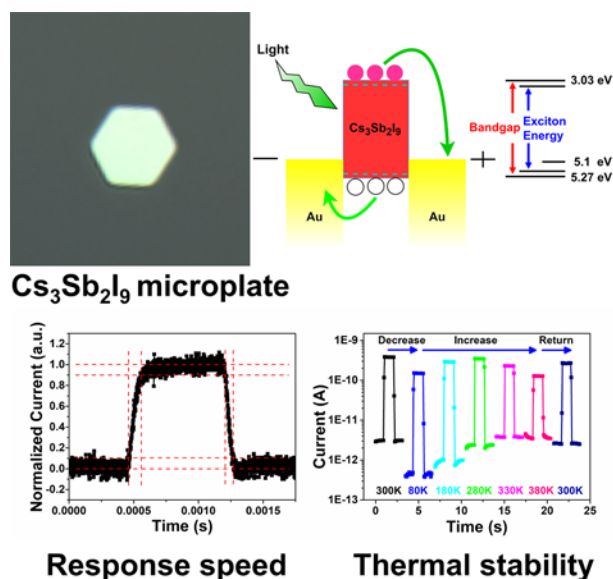
² Department of Materials Science and Engineering, City University of Hong Kong, Kowloon, Hong Kong SAR

³ Department of Physics, Khulna University of Engineering & Technology (KUET), Khulna, Bangladesh

⁴ State Key Laboratory of Luminescence and Applications, Changchun Institute of Optics, Fine Mechanics and Physics, Chinese Academy of Sciences, 3888 Dongnanhu Road, Changchun 130021, China

⁵ State Key Laboratory of Terahertz and Millimeter Waves, City University of Hong Kong, Kowloon, Hong Kong SAR

⁶ Department of Physics, Comilla University, Kotbari, Comilla 3506, Bangladesh



All-inorganic and lead-free $\text{Cs}_3\text{Sb}_2\text{I}_9$ perovskite microplates are successfully synthesized by a two-step chemical vapor deposition method. Photoconductive devices fabricated using these microplates exhibit the ultra-fast response speed and superior thermal stability to function reversibly with a wide temperature range between 80 K and 380 K.

Johnny C. Ho <https://hocityu.com/>

Crystalline All-Inorganic Lead-Free Cs₃Sb₂I₉ Perovskite Microplates with Ultra-Fast Photoconductive Response and Robust Thermal Stability

Sujit Kumer Shil,^{1,3,§} Fei Wang,^{2,4,5,§} Zhengxun Lai,² You Meng,² Yunpeng Wang,⁴ Dongxu Zhao,⁴ Mohammad Kamal Hossain,^{1,6} Kingsley O. Egbo,¹ Ying Wang,¹ Kin Man Yu,¹ and Johnny C. Ho^{2,5}

¹ Department of Physics, City University of Hong Kong, Kowloon, Hong Kong SAR

² Department of Materials Science and Engineering, City University of Hong Kong, Kowloon, Hong Kong SAR

³ Department of Physics, Khulna University of Engineering & Technology (KUET), Khulna, Bangladesh

⁴ State Key Laboratory of Luminescence and Applications, Changchun Institute of Optics, Fine Mechanics and Physics, Chinese Academy of Sciences, 3888 Dongnanhu Road, Changchun 130021, China

⁵ State Key Laboratory of Terahertz and Millimeter Waves, City University of Hong Kong, Kowloon, Hong Kong SAR

⁶ Department of Physics, Comilla University, Kotbari, Comilla 3506, Bangladesh

[§] Sujit Kumer Shil and Fei Wang contributed equally to this work.

Received: day month year

Revised: day month year

Accepted: day month year
(automatically inserted by
the publisher)

© Tsinghua University Press
and Springer-Verlag Berlin
Heidelberg 2014

KEYWORDS

All-inorganic, lead-free
perovskite, Cs₃Sb₂I₉,
microplates,
photoresponse, stability

ABSTRACT

Hybrid organolead halide perovskites have attracted tremendous attention due to their recent success as high efficiency solar cell materials and their fascinating material properties uniquely suitable for optoelectronic devices. However, the poor ambient and operational stability as well as the concern of lead toxicity greatly hamper their practical utilization. In this work, crystalline, all-inorganic and lead-free Cs₃Sb₂I₉ perovskite microplates are successfully synthesized by a two-step chemical vapor deposition method. As compared with other typical lead-free perovskite materials, the Cs₃Sb₂I₉ microplates demonstrate excellent optoelectronic properties, including substantial enhancements in the Stokes shift, exciton binding energy and electron-phonon coupling. Simple photoconductive devices fabricated using these microplates exhibit an ultra-fast response with the rise and decay time down to 96 μs and 58 μs, respectively. This respectable photoconductor performance can be regarded as a record among all the lead-free perovskite materials. Importantly, these photodetectors show superior thermal stability in a wide temperature range, capable to function reversibly between 80 K and 380 K, indicating their robustness to operate under both low and high temperatures. All these results evidently suggest the technological potential of inorganic lead-free Cs₃Sb₂I₉ perovskite microplates for next-generation high-performance optoelectronic devices.

Address correspondence to Fei Wang, wangf@ciomp.ac.cn; Kin Man Yu, kinmanyu@cityu.edu.hk; Johnny C. Ho, johnnyho@cityu.edu.hk

Introduction

In past decades, photodetectors have been developed into one of mature technological products for the conversion of incident optical information into electrical signals.[1, 2] They are not only essential devices in conventional technologies, including communication, imaging, environmental monitoring and target detection, but also have a huge application potential in emerging areas, such as object recognition for self-driving vehicles, artificial intelligence and internet-of-things systems.[2, 3] The recent advent of hybrid organolead halide perovskite (ABX_3 with A = organic cation, B = Pb and X = halide) as materials with properties uniquely suitable for high efficiency solar cells and many optoelectronic devices[4–13] provides the opportunity to further enhance the performance of photodetectors using halide perovskites. For instance, using solution-processed $CH_3NH_3PbI_3$ films as device channels, Hu et al. fabricated broadband wavelength photodetectors (from ultraviolet to visible) with the photoresponsivity of 3.49 AW^{-1} , 0.0367 AW^{-1} and external quantum efficiency of $1.19 \times 10^3\%$, 5.84% at 365 nm and 780 nm irradiation wavelength, respectively.[6] Dou and his team later demonstrated another high-performance photodetector utilizing $CH_3NH_3PbI_{3-x}Cl_x$ films, covering a linear dynamic range over 100 decibels (dB), with an enhanced detectivity up to 10^{14} Jones and fast photo response with 3-dB bandwidth approaching 3 MHz.[7] These examples demonstrated that symmetrically structured photoconductive detectors with the excellent performance could be achieved using organometal halide perovskites.[14]

Although the detectivity and responsivity of hybrid perovskite photodetectors are superior to other photodetectors, they tend to be unstable during long term operation in ambient air and temperature.[15–17] These instabilities are mostly attributed to the low thermal decomposition temperature and extreme sensibility of organic cations (A) to moisture.[18–21] At the same time, the concern of the toxicity of Pb would inevitably limit these Pb-based perovskites for practical utilization. Hence, there has been an extensive search for environmental-friendly lead-free all-inorganic perovskites for photodetector fabrication with the aims to improve both device stability as well as performance.[22–24] Typically, the unstable organic cation group can be replaced by a monovalent metal cation (e.g. Cs^+ or Rb^+). However, choices of non-toxic B ions to replace Pb are severely limited by the narrow range of the Goldschmidt tolerance

factor for a closed packed perovskite structure.[25, 26] With the similar atomic radius of Pb, Sn has been once considered as the promising alternative for Pb-free perovskites,[27, 28][29] but the rapid oxidation of Sn^{2+} to Sn^{4+} makes the Sn-based perovskites very unstable in ambient. Lately, there is a new class of defect-ordered perovskites with exceptional stability with the structure of $A_3M_2X_9$ that can be derived by replacing a portion of the metal sites of conventional ABX_3 perovskites by vacancies. Here, M denotes Bi^{3+} or Sb^{3+} ions occupying 2/3 of the B sites in ABX_3 perovskites.[5, 30–33] In particular, solution-processed $Cs_3Sb_2I_9$ perovskite thin films have been explored for light emitting[34, 35] and photovoltaic applications.[32, 36, 37] However, due to the poor crystallinity and high trap-state density in solution-processed materials, the device performance of $Cs_3Sb_2I_9$ based optoelectronic devices are far from acceptable.[5, 30, 38] Although solution process is a facile and common way to fabricate perovskite materials, the different solubilities of precursors in solvents make them hard to react proportionally and uniformly, hindering the obtained crystallinity of the reaction products. As compared with the solution-processed materials, chemical vapor deposition (CVD) is a well-established method to achieve excellent optoelectronic materials, especially for micro- and nanostructures with improved surface-to-volume ratio for the better photodetector performance. However, due to the extreme disparity in the melting temperature for CsI (621°C) and SbI₃ (171°C), synthesis of high-quality $Cs_3Sb_2I_9$ materials using the CVD process is a formidable task.

In this work, in order to overcome the challenges to growth high quality $Cs_3Sb_2I_9$ by conventional CVD method, we developed a two-step CVD process and successfully synthesized highly-crystalline, all-inorganic and Pb-free $Cs_3Sb_2I_9$ microplates. The $Cs_3Sb_2I_9$ microplates exhibit substantial enhancements in the Stokes shift, exciton binding energy and electron-phonon coupling over other perovskite structures. Photoconductive devices fabricated using these $Cs_3Sb_2I_9$ microplates deliver a respectable performance with responsivity up to 40 mA/W and on/off current ratio reaching 10^4 at 532 nm irradiation wavelength. More importantly, their rise and decay times can be down to $96\text{ }\mu\text{s}$ and $58\text{ }\mu\text{s}$, respectively, constituting a record fast response among all Pb-free perovskite photoconductive devices. These $Cs_3Sb_2I_9$ microplate devices also demonstrated superior thermal stability within a wide temperature range, spanning reversibly from 80 K all the way to 380 K . All these results evidently provide a simple but effective way to achieve crystalline, all-inorganic and lead-free perovskites

for high-performance and robust optoelectronic devices.

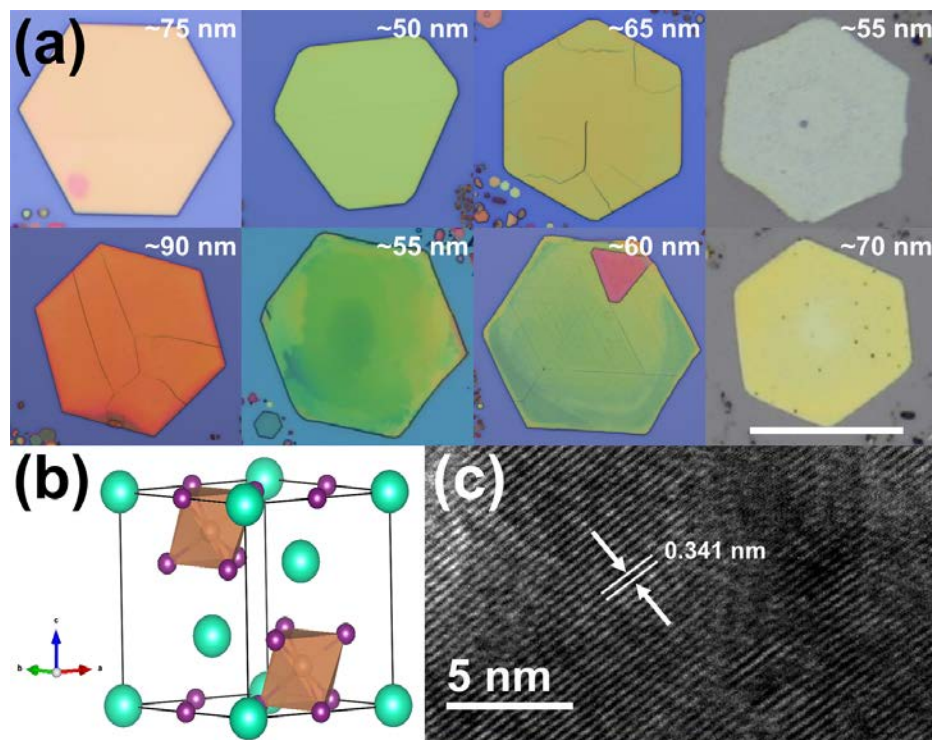


Figure 1. (a) Optical images of the microplates formed on the Si substrates (coated by 250 nm SiO₂, purple background) and sapphire substrates (gray background), showing the homogeneous distribution of crystal morphologies and sizes. The different colors of the microplates are originated from their different thicknesses. Scale bars are 10 μ m. (b) An illustration of the atomic model of a Cs₃Sb₂I₉ unit cell. (c) A HRTEM image of the microplate.

Results and Discussion

Cs₃Sb₂I₉ perovskite microplates were grown in a single zone tube furnace by using a two-step CVD approach. The schematic of the overall synthesis strategy of Cs₃Sb₂I₉ perovskite microplates is illustrated in **Figure S1a**. The process details are described in the Method section, while the microplate evolution is investigated by scanning electron microscopy (SEM) after each process step as depicted in Figure S1b-d. To be specific, the optimized CsI films were first grown on Si substrates in step-I (Figure S1b). Then, the SbI₃ precursor layer was deposited over the CsI film for the subsequent formation of microplates in step-II (Figure S1c). Since the melting temperature of CsI is relatively high (621 $^{\circ}$ C), the deposition of SbI₃ precursor on the CsI film at a much lower temperature (130 $^{\circ}$ C) would simply make the crystallization reaction process more uniform and stoichiometric. The uniform crystallization process induces the formation of SbI₃ microplates, instead of continuous SbI₃ films, without deteriorating the material quality of the underlying CsI film. An SEM image of SbI₃ microplates grown directly on the sapphire substrate under the same condition is

given in Supporting Information **Figure S2**. The same SbI₃ microplate morphology obtained shows that the as-prepared CsI film does not affect the deposition of the SbI₃ precursor. After the two step depositions, the sample was annealed at 180 $^{\circ}$ C in the tube furnace in flowing N₂. During the annealing process, due to the lower melting point of SbI₃, the SbI₃ microplates would function as precursor sources to react with the CsI film. After the recrystallization, Cs₃Sb₂I₉ perovskite microplates with a hexagonal shape were achieved on the substrate (**Figure 1a** and Figure S1d), showing the homogeneous distribution of crystal morphologies and sizes. We note that the Cs₃Sb₂I₉ microplates were not defined or inherited from the SbI₃ microplates, and the edge lengths of the microplates are 5 to 10 μ m. This two-step CVD method can provide a simple and effective way to synthesize large-scale perovskite microplates for the subsequent device fabrications.

The crystal structure and chemical composition of the obtained perovskite microplates were first characterized. Detailed crystallographic data are given in **Table S1** in Supporting Information and the unit cell and 2D layered structure of Cs₃Sb₂I₉ perovskite are shown schematically in Figure 1b

and Supporting Information **Figure S3**. The $\text{Cs}_3\text{Sb}_2\text{I}_9$ perovskite consists of bi-octahedral $(\text{Sb}_2\text{I}_9)^{3-}$ clusters that are surrounded by Cs cations to achieve the charge balance. The unit cell has a trigonal phase with the space group of $P\bar{3}m1$ (164) with lattice parameters of $a = b = 8.42 \text{ \AA}$, $c = 10.386 \text{ \AA}$, and angles of $\alpha = \beta = 90^\circ$, $\gamma = 120^\circ$. X-ray diffraction (XRD) measurements (**Figure 2**) reveal the crystalline nature of the $\text{Cs}_3\text{Sb}_2\text{I}_9$ perovskite microplates, with diffraction peaks indexed to the 2D layered $\text{Cs}_3\text{Sb}_2\text{I}_9$ perovskite structure (JCPDS No. 88-0690). Even after one-month ambient exposure without any capsulation (Temperature: $\sim 26^\circ\text{C}$, Humidity: 60–70 %), the XRD pattern does not show any noticeable change, indicating the excellent stability of these microplates in oxygen and moisture

environment at room temperature (**Figure 2a**). High resolution XRD of the (201) peak (**Figure 2b**) shows that the (201) peak is rather sharp and symmetric without any shoulders, indicating the good phase purity of the $\text{Cs}_3\text{Sb}_2\text{I}_9$ microplates. The corresponding rocking curve (**Figure 2c**) further reveals a relatively narrow full-width-half-maximum (FWHM) of 0.145° , which confirms the excellent crystallinity of the microplates. Also, **Figure S4** presents the XRD patterns of precursor layers (CsI only and SbI_3 only) grown under the same CVD condition mentioned above. They don't share any peaks with the patterns in **Figure 2a**, indicating the absence of impurities and residual raw materials in the $\text{Cs}_3\text{Sb}_2\text{I}_9$ microplates.

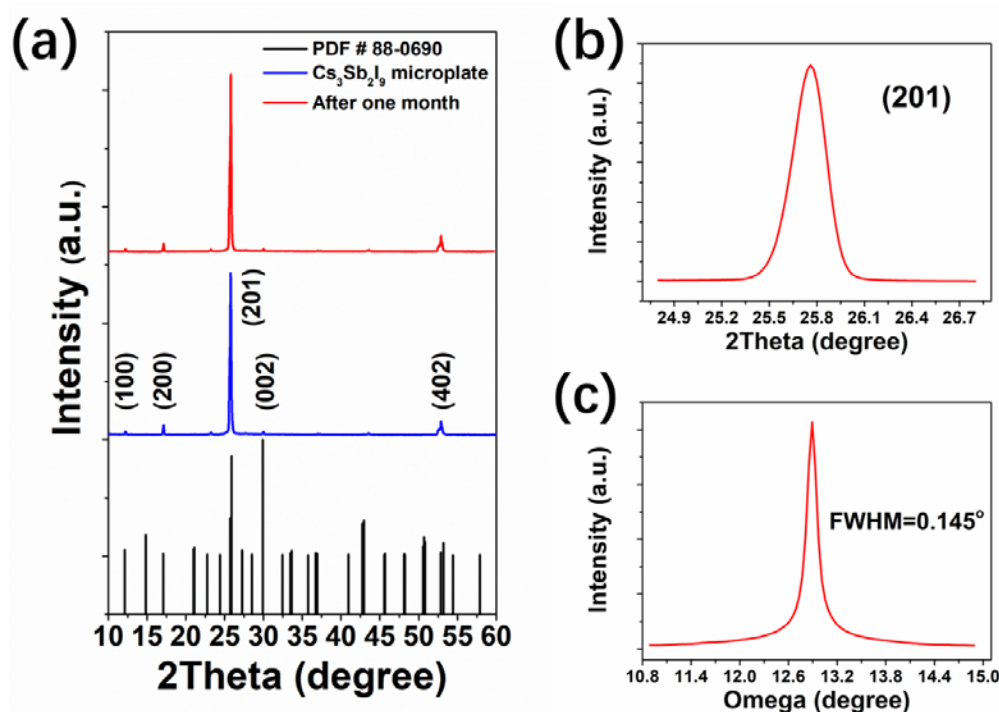


Figure 2. XRD patterns (a), high-resolution XRD spectrum (b) and the corresponding rocking curve (c) of the microplates.

The highly crystalline nature of the microplates is further confirmed by the high-resolution transmission electron microscopy (HRTEM) image of the sample (**Figure 1c**) which clearly shows lattice fringes with a spacing of 0.341 nm , corresponding to the (201) plane of the $\text{Cs}_3\text{Sb}_2\text{I}_9$ crystal. The thickness of the microplates was studied by atomic force microscopy (AFM), which shows a distribution of thicknesses between 50 to 100 nm (Supporting Information **Figure S5**). In addition, the elemental composition of these $\text{Cs}_3\text{Sb}_2\text{I}_9$ microplates was analyzed by using energy dispersive X-ray spectroscopy (EDX). In the EDX spectrum from a microplate, strong signals from Cs,

Sb and I with the atomic ratios (%) of Cs:Sb:I = 22.1:15.7:62.2 are observed, consistent with the expected stoichiometric ratio of $\text{Cs}_3\text{Sb}_2\text{I}_9$ perovskite (Supporting Information **Figure S6**). Notably, these microplates have a relatively uniform distribution of their constituents as supported by the corresponding elemental mappings (Supporting Information **Figure S7**). All these results confirm the crystallinity, crystal phase-purity and chemical stoichiometry of $\text{Cs}_3\text{Sb}_2\text{I}_9$ perovskite microplates grown by the two-step CVD process.

UV-vis absorption and photoluminescence (PL) measurements were carried out to examine the bandgap and luminescent characteristics of $\text{Cs}_3\text{Sb}_2\text{I}_9$

perovskite microplates. Based on the absorption spectrum, there is an absorption peak located at 556 nm, which can be considered as the 1st exciton absorption peak (Figure 3a). This exciton peak is then followed by an absorption edge, attributed to the band to band photon absorption. Using the Tauc plot, a bandgap energy of 2.24 eV can be determined for these perovskite microplates (Supporting Information Figure S8). An exciton binding energy of ~230 meV can be estimated from the edges of the bandgap and exciton absorption. Meanwhile, by fitting the absorption spectrum with the quantum-well absorption model modified for nanoplates or nanosheets,[39, 40] we obtain an exciton binding energy of 282 meV (fitting method and results shown in Supporting Information Figure S9), in good agreement with the experimental value determined above. This exciton binding energy for Cs₃Sb₂I₉ microplates is slightly lower than that reported for Bi-based perovskites (e.g. A₃Bi₂I₉ with energy value of 300~400 meV),[38, 41] but much higher than those for Pb-based perovskites and other semiconductor materials. Devices fabricated from materials with high exciton binding energy can maintain good device performance under large electric fields, high temperature and intense irradiation conditions. Hence, the high exciton binding energy of Cs₃Sb₂I₉ microplates suggests that they are potential candidates for optoelectronic devices operating in harsh environments. Moreover, the PL peak of the

microplates is found to locate at 640 nm, whereas the peak sharpness indicates the good crystallinity of the samples. In this case, there is a strong Stokes shift of approximately 520 meV between the absorption edge and the PL emission. This Stokes shift value is much higher than other semiconductor materials.[42, 43] In contrast, typical lead halide perovskites have small Stokes shift (30~70 meV) which gives rise to a strong self-absorption effect,[42, 44] severely restricting their light outcoupling efficiency.[42] The relatively large Stokes shift of the Cs₃Sb₂I₉ microplates would make them as attractive active materials for high-performance light emitting and laser diodes. Notably, copper-based halides perovskites have even larger exciton binding energies (335~490 meV for Cs₃Cu₂I₅[45, 46]; ~205 meV for CsCu₂I₃[47, 48] and ~700 meV for Ru₂CuBr₃[42]) and Stokes shifts (161~238 nm for Cs₃Cu₂I₅; ~210 nm for CsCu₂I₃ and ~85 nm for Ru₂CuBr₃, respectively). Benefitting from the small self-absorption and efficient light out-coupling, high radioluminescence yields were observed within these materials.[42, 45-48] However, such large exciton binding energy could also lead to the difficulty of exciton dissociation in the materials, which generally result in a higher dark current and lower light current.[49, 50] Therefore, for achieving high-performance photon-electron conversion devices operating under high temperatures, materials with a moderate exciton binding energy is more desirable.

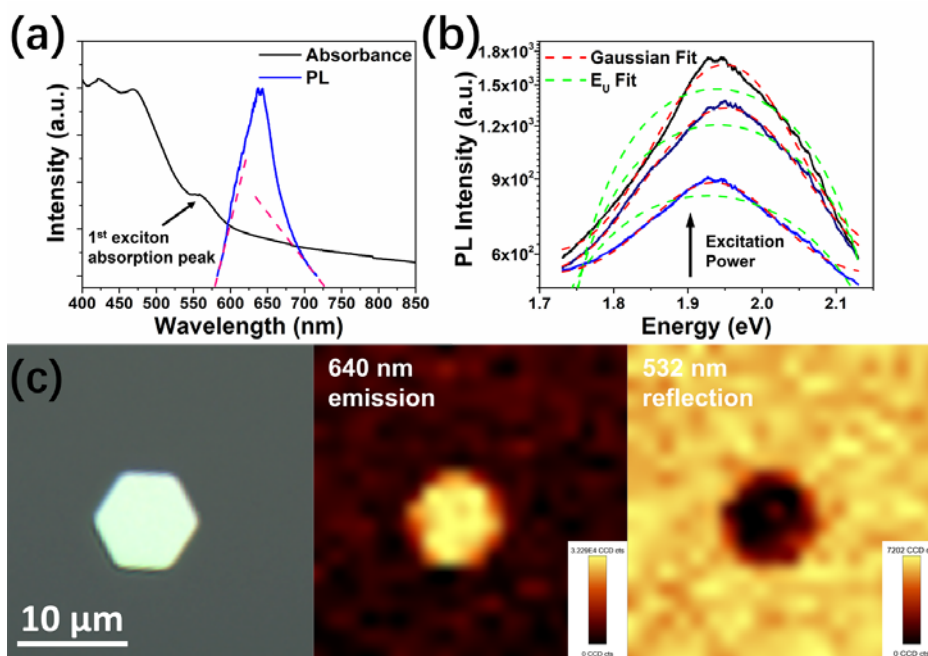


Figure 3. (a) UV-vis absorption and steady-state PL spectra of the Cs₃Sb₂I₉ microplates. (b) PL spectra under different exciting powers ($\lambda_{\text{excitation}} = 532$ nm) and corresponding fitted curves. (c) Steady-state PL mapping of a typical Cs₃Sb₂I₉ microplate.

It is also worth noting that the PL emission peak of the Cs₃Sb₂I₉ microplates has an asymmetrical shape, with the slope of the peak at the low-energy (longer wavelength) side being much smaller than that of the high-energy (shorter wavelength) side (Figure 3a). This asymmetry of the peak shape can reflect the skewness and fluctuation of local potentials in the crystal, which suggests the presence of a strong electron-phonon coupling. Technically, a strong electron-phonon coupling in materials would lead to the charge localization and emission of phonons, followed by the altered energy of emitted photons.[51] In this manner, the low-energy tail of the PL peak observed for Cs₃Sb₂I₉ microplates is an indication of electron-phonon couplings in the material. In order to further evaluate electron-phonon couplings in these Cs₃Sb₂I₉ microplates, we use the theory of Toyozawa[51, 52] in which the PL peak width, $W(T)$, was related to the average phonon energy, electron-photon coupling and other parameters via the following expressions:

$$W(T) = 2.36\sqrt{S}E_{ph} \left[\coth\left(\frac{E_{ph}}{2k_B T}\right) \right]^{\frac{1}{2}} \quad (1)$$

$$S = \frac{W(T)^2}{5.5696E_{ph}^2 \coth\left(\frac{E_{ph}}{2k_B T}\right)} \quad (2)$$

where S is the Huang–Rhys electron–phonon coupling parameter, k_B is the Boltzmann constant, T is the temperature and E_{ph} is the effective phonon energy. The E_{ph} value of Cs₃Sb₂I₉ materials is calculated to be 7.0 ± 0.8 meV.[51] PL measurements were performed on Cs₃Sb₂I₉ microplates with increasing excitation power densities (Figure 3b) and the PL spectra were analyzed using Eq. (1) and (2). Best fits with Gaussian functions of the spectra reveals a $W(T) = 0.19 \pm 0.014$ eV at 300 K for the Cs₃Sb₂I₉ microplates, giving rise to a S parameter of 17.88 ± 5.0 . This S parameter value is higher than the reported value for CsX (e.g. 4.8, 3.7 and 12 for Cl, Br and I, respectively),[53, 54] demonstrating the much stronger electron-phonon coupling of the Cs₃Sb₂I₉ microplates. Furthermore, there is also an exponential tail at the lower energy side of the absorption spectrum. This tail is known as Urbach tail that is resulted from the intrinsic electron-phonon coupling.[55, 56] The value of Urbach energy, E_U , can be estimated by the van Roosbroeck-Shockley relationship:[56, 57]

$$\alpha(E, T) \propto \exp\left(\frac{E}{E_U}\right) \quad (3)$$

$$I_{PL}(E, T) \propto \alpha(E, T)E^2 \exp\left(\frac{E}{-k_B T}\right) \quad (4)$$

where $I_{PL}(E, T)$ and $\alpha(E, T)$ are the PL and absorption spectra, respectively. The relationship between $I_{PL}(E, T)$ and E_U can then be described in the following expression:

$$I_{PL}(E, T) = AE^2 \exp\left(\frac{E}{E_U} - \frac{E}{k_B T}\right) \quad (5)$$

where A is a constant. By fitting the experimental spectra with Eq. (5), the E_U value is estimated to be 26.5 ± 0.005 meV, which is much higher than that for CsPbBr₃ (14 meV), MAPbBr₃ (15 meV) and FAPbBr₃ (17 meV).[56] This further confirms the stronger electron-phonon coupling of the Cs₃Sb₂I₉ microplates, which gives rise to the electric dipole moments, the coupling to the electric field of plasmons and the longitudinal collective excitations of electron gas.[58]

Furthermore, PL mapping of the Cs₃Sb₂I₉ microplates was also performed. As observed in the mapping of a typical microplate shown in Fig. 3c, PL emission mainly occurs from the hexagonal Cs₃Sb₂I₉ microplate, with stronger intensities from the inner region of microplate than the edges and corner regions of the hexagon (Supporting Information **Figure S10**). This spatial intensity variation is possibly caused by the relatively low specific surface area and low surface defect density of the microplate. Moreover, the low reflection of the exciting beam from the hexagonal plate also indicates the good absorbance of the Cs₃Sb₂I₉ microplate. The charge recombination properties of the microplates are revealed by time-resolved PL measurements. As shown in Supporting Information **Figure S11**, the PL decay curve can be well fitted by a biexponential decay model with a short lifetime (τ_1) of 5.9 ns and a long lifetime (τ_2) of 24.3 ns, respectively. The fast decay rate of PL intensity indicates that the faster exciton recombination dominates over the slower transitions at defect states.[35] These findings illustrate the excellent optical properties of Cs₃Sb₂I₉ microplates, making them uniquely suitable for various optoelectronic devices.

To demonstrate the practical utilization of these Cs₃Sb₂I₉ microplates, we fabricate simple photoconductive devices and performed detailed performance evaluation studies on these devices. **Figure 4a** shows a schematic diagram of the

microplate photodetector with thermally evaporated Au electrodes deposited 10 μm apart on the microplate by using Ni grids (300 mesh) as shadow masks. Before performing any device measurement, the valence band maximum of $\text{Cs}_3\text{Sb}_2\text{I}_9$ was measured by ultraviolet photoelectron spectroscopy (UPS) to be 5.27 eV (Fig. 4b). The corresponding energy band alignment of the $\text{Cs}_3\text{Sb}_2\text{I}_9$ microplate photodetector is shown in Figure 4c, suggesting that Au with a typical work function of 5.1 eV is an appropriate metal to serve as efficient electrical contacts for the photodetector. The Hall mobility of the $\text{Cs}_3\text{Sb}_2\text{I}_9$ material is $\sim 33 \text{ cm}^2/\text{Vs}$ with the p-type conductivity, while the tested carrier density is found to be $\sim 4 \times 10^{13} \text{ cm}^{-3}$. Then, the current-voltage (I-V) characteristics of $\text{Cs}_3\text{Sb}_2\text{I}_9$ microplate devices were measured to reveal their electrical properties. Figure 4d and e present the I-V curves of the device in the dark and under 532 nm light illumination with increasing power densities. It is seen that the microplate device

has a high resistance with a dark current of around several pA in the dark. Yet, under illumination, the output current increases by several orders of magnitude. Also, the linear I-V curves imply that there is an ohmic-like contact formed between Au electrodes and $\text{Cs}_3\text{Sb}_2\text{I}_9$ channels, whereas the increase of current indicates the device being sensitive to incident 532 nm photons. Figure 4f shows the successive on/off switching characteristics of the device at 1 V bias upon 532 nm light illumination. At the very instant of illumination, the current increases rapidly over 3 orders of magnitude without any noticeable degradation over repeated switching cycles. With an applied bias of 0.5 V, the on/off ratio between photo- and dark-current can reach up to 4 orders of magnitude (Supporting Information Figure S12). However, the device dark current at 0.5 V bias increases slowly after several on/off cycles. For stable performance, the optimized operating bias of 1 V is needed for the device.

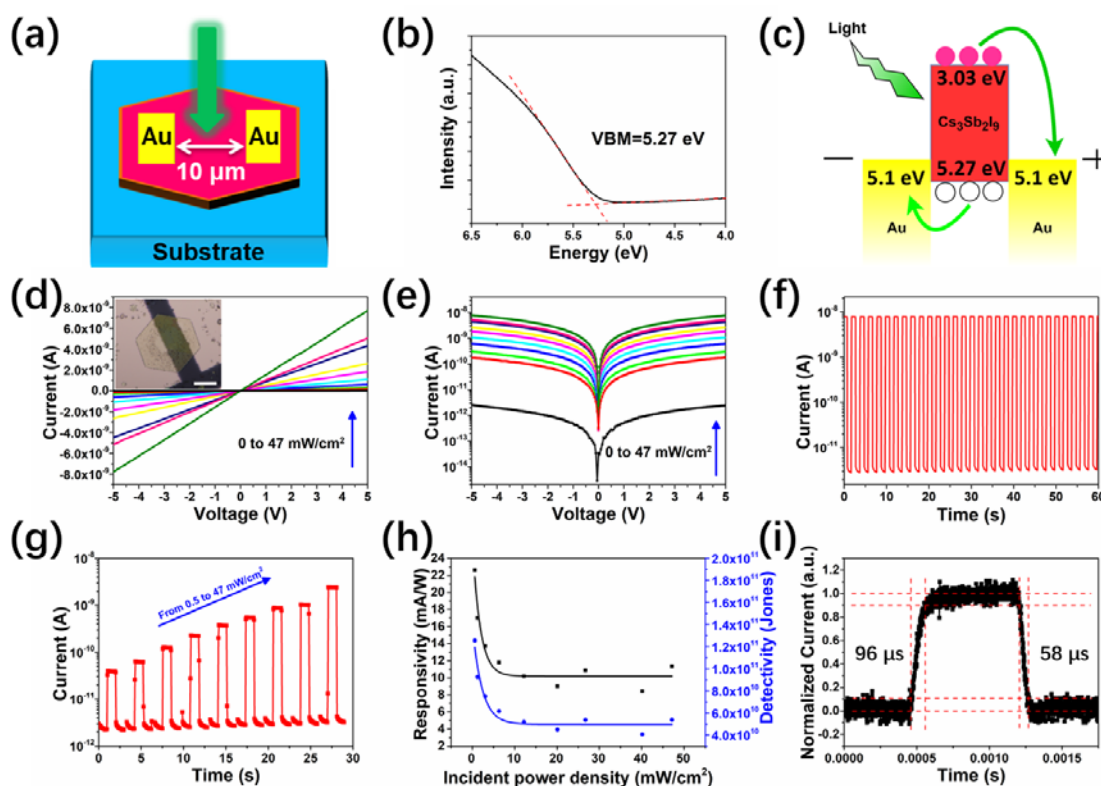


Figure 4. (a) A schematic illustration of the $\text{Cs}_3\text{Sb}_2\text{I}_9$ microplate photodetector. (b) A UPS spectrum showing the valence band minimum (VBM) value of the $\text{Cs}_3\text{Sb}_2\text{I}_9$ microplate. (c) A schematic showing the energy band alignment and light induced carriers transport in the photodetector. (d) and (e) I-V characteristics of the device in the dark and under illumination, respectively. The inset of (d) shows the optical image of the device. The scale bar is 10 μm . (f) The reproducible on/off switching of the device under the incident power density of 47 mW/cm^2 . (g) The photocurrent of the device upon various incident power intensities. (h) Power dependent responsivity and detectivity curves of the device. (i) Response of the device to pulsed 532 nm light irradiation at a frequency of 800 Hz under 1 V bias.

Since the relationship between photocurrent and light intensity can serve as a direct evidence to assess the performance stability of a photodetector under both weak and strong signals, the photosensitivity dependence of the device on various incident power densities is hence explored. Figure 4g shows that the photocurrent rises proportionally with the increasing power intensities from 0 to 47 mW/cm² under 532 nm light illumination, which suggests that more incident photons can generate more photo-carriers in the device. As a critical parameter to characterize the performance of photodetectors, the responsivity (R) of the device is defined as:

$$R = \frac{I_{ph}}{L_{light}} \quad (6)$$

where I_{ph} is the photocurrent and L_{light} is the effective power of incident light illuminated on the device. The inset of Figure 4d shows that actual dimension of a typical device and its active area is determined to be 3×10^{-6} cm². The responsivity of the device is plotted in Figure 4h as a function of the incident power density. The device responsivity has the highest value of 23 mA/W at a low incident

power density of 0.5 mW/cm², followed by a rapid decay with the increasing incident power density to a stable value of ~ 10 mA/W for power intensity > 10 mW/cm². Because more charge recombination occurs under higher illumination intensity, the lowest-lying trap states with the longest lifetime that provide the highest photoconductive gain at low intensities are filled, resulting in the decrease of the responsivity.[59][60] As the number of illumination photons increases, the absorption gradually saturates in the microplates. Consequently, the photo-generated carriers and the charge recombination reach a dynamic equilibrium, resulting in the steady value under higher illumination. To further characterize the weakest level of light that the detector can operate, detectivity (D^*) is determined by the responsivity R and the dark current I_D with the following expression:

$$D^* = \sqrt{\frac{A}{2qI_D}} R \quad (7)$$

where I_D is the dark current, q is the elementary charge and A is the effective area. Similarly, the maximum detectivity value at the low incident

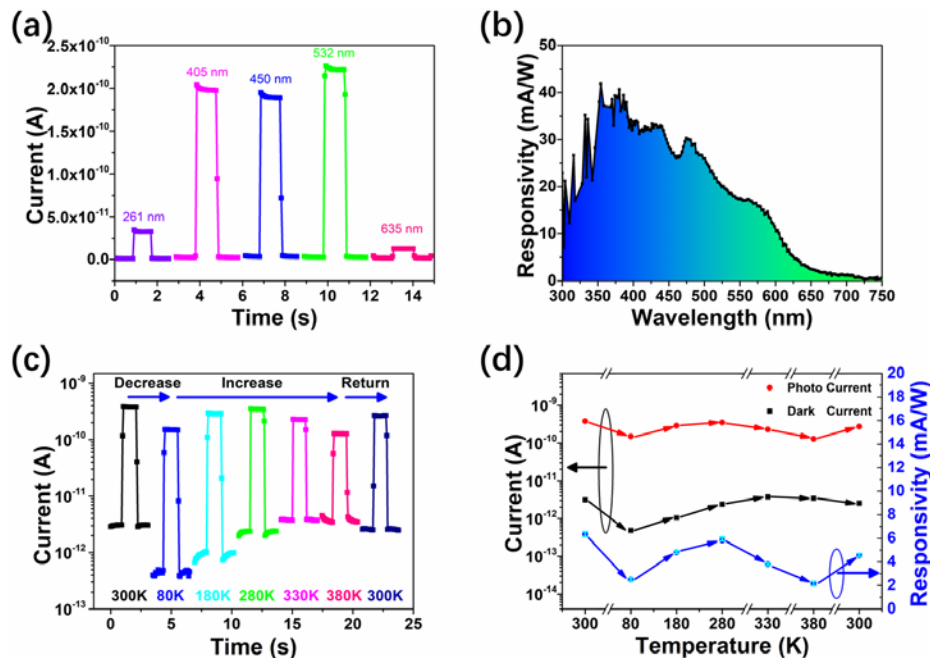


Figure 5. (a) Room temperature spectral photocurrent and (b) responsivity of the Cs₃Sb₂I₉ microplate device. (c) Temperature dependent photoresponse and (d) responsivity of the device with the incident wavelength of 532 nm. The measurements were performed under 1 V bias with an incident power density of 20 mWcm⁻².

power density of 0.5 mW/cm^2 is found to be 1.26×10^{11} Jones ($\text{cmHz}^{1/2}\text{W}^{-1}$), which decreases to a stable value of $\sim 5 \times 10^{10}$ Jones at $>10 \text{ mW/cm}^2$ incident power (Figure 4h). Another important parameter characterizing a photodetector is its on/off switching characteristics. The device response time was measured with the 532 nm light source by using a chopper to turn the illumination on and off on the device. The rise time, defined as the time for the current to increase from 10 % to 90 % of its peak value, is determined to be 96 μs . Likewise, the decay time, described as the time for the current to decrease from 90 % to 10 % of its peak, is found to be 58 μs . These efficient rise and decay time constants of $\text{Cs}_3\text{Sb}_2\text{I}_9$ microplate devices are already better than other state-of-the-art Pb-free perovskite photodetectors. Performance parameters of photodetectors fabricated from Pb-free perovskite materials reported previously are compiled in **Table 1** and compared with our $\text{Cs}_3\text{Sb}_2\text{I}_9$ microplate devices. These rapid response and recovery speeds of the device arises from the fast separation and effective extraction of photo-generated electron-hole pairs in the material, which can be ascribed to the excellent crystal quality of $\text{Cs}_3\text{Sb}_2\text{I}_9$ microplates.

Apart from the response time, it is also essential to evaluate the photoresponse of detectors to different incident wavelengths. As shown in **Figure 5a**, the $\text{Cs}_3\text{Sb}_2\text{I}_9$ microplate device is capable of responding efficiently to the illumination of photons with different wavelengths λ with different photocurrent values. It is clear that the magnitude of photocurrent depends heavily on the light absorption of device active materials. Therefore, we expect to have high photocurrents for above bandgap irradiation with 405 nm to 532 nm photons. The spectral responsivity curve of the device is measured and illustrated in Figure 5b. Note that the device maintains a high responsivity with incident photons with λ ranging from 350 nm to 550 nm, and then the responsivity decreases dramatically for photons with $\lambda > 600 \text{ nm}$. This spectral responsivity follows the absorption characteristics and the exciton absorption edge of $\text{Cs}_3\text{Sb}_2\text{I}_9$ microplates as depicted in Figure 3a. The absorption tail which extends from 600 nm to 800 nm results in a low photocurrent obtained at $\lambda \sim 635 \text{ nm}$ (Figure 5a). The spectral range and magnitude of the responsivity curve can be further manipulated by tailoring the optical absorption properties via controlling the composition of the cation and anion halides in all-inorganic lead-free $\text{A}_3\text{M}_2\text{X}_9$ perovskites.

As mentioned earlier, the stability (thermal and ambient) issue of perovskite devices, in particular organic hybrid halide perovskite devices is still a challenging hurdle. In order to examine the thermal stability of $\text{Cs}_3\text{Sb}_2\text{I}_9$ microplate photodetectors, the

device performance was investigated in the temperature range of 80 to 380 K under 1 V bias with an incident photon wavelength of 532 nm and a power density of 20 mW/cm^2 . As displayed in Figure 5c and d, both the photo- and dark-current reduce with decreasing temperature. The photocurrent decreases from 379 pA at 300 K to 150 pA at 80 K, while the dark current shows the same tendency from 3 pA to 0.4 pA. Such decreases in currents may be associated with the restricted ion migration at low temperatures. Obviously, the decrease rate of the dark current is slightly faster than that of the photocurrent, resulting in an enhancement of on/off current ratio. In fact, as the temperature goes from 80 K to 280 K, the conductance of $\text{Cs}_3\text{Sb}_2\text{I}_9$ microplates increases. Thus, both photo- and dark-current exhibit the positive correlation with operating temperature. However, with increasing temperature above 280 K, the photocurrent decreases again, while the dark current remains relatively stable. This behavior is different from the previously reported results in lead-based perovskites which showed that both photo- and dark-current rise rapidly with increasing temperature.[72] This may be the effect of the large exciton binding energy of $\text{Cs}_3\text{Sb}_2\text{I}_9$ microplates, which can effectively maintain their carriers at high temperatures. Moreover, the reproducibility of the on/off switching of the device was also measured in the temperature range of 80 K and 380 K and the device demonstrates excellent repeatability and invariable photoresponse to the incident irradiation (Supporting Information **Figure S13**). Temperature cycling study shows that the photocurrent and responsivity can recover to more than 70 % of their initial values after heating up to 380 K and then cooling back down to room temperature. This indicates that the device has enhanced high tolerance to both low and high temperatures (Figure 5d). The long-term stability of $\text{Cs}_3\text{Sb}_2\text{I}_9$ microplate photodetectors was further evaluated by retesting the devices after they were stored for 100 days in ambient air and moisture. We notice that the dark current of the device gradually increases from 10^{-11} to 10^{-10} A , while the photocurrent decreases slightly as well (Supporting Information **Fig. S14**). In any case, the device still maintains an on/off current ratio of 100 with the corresponding responsivity of 9.7 mA W^{-1} , which is $\sim 85\%$ of its initial value.

Conclusion

In summary, we have successfully synthesized crystalline, all-inorganic and Pb-free $\text{Cs}_3\text{Sb}_2\text{I}_9$ perovskite microplates using a two-step CVD approach. The obtained microplates show a large stokes shift of 520 meV, a large exciton binding energy of 282 meV and an improved

electron-phonon coupling. When these microplates are configured into photoconductive devices, they exhibit a respectable responsivity up to 40 mA W^{-1} and detectivity reaching 10^{11} Jones at 532 nm irradiation wavelength. Notably, benefiting from the excellent crystalline quality of microplates, the photodetectors achieve ultra-fast photoresponse with rise and decay times as low as 96 μs and 58 μs , respectively. More importantly, due to the

enhanced exciton binding energy, the photodetectors also exhibit superior stability under both low and high temperatures. Our findings on the materials properties and photodetector performance strongly suggest that $\text{Cs}_3\text{Sb}_2\text{I}_9$ is an all-inorganic Pb-free perovskite material which will have huge application potentials for photodetectors and other optoelectronic devices.

Table 1. A comparison of performance parameters of photodetector fabricated using various Pb-free halide perovskite materials.

Material	Method/ Morphology	Responsivity (mA W^{-1})	Detectivity (Jones)	Highest On/off ratio	Rise/decay time (ms)	Ref.	Date
$\text{CH}_3\text{NH}_3\text{SnI}_3$	CVD/ Nanowire	470	8.8×10^{10}	N/A	1500/400	[61]	2017
$\text{CsBi}_3\text{I}_{10}$	Solution/ Thin film	21800	1.93×10^{13}	10^5	0.33/0.38	[23]	2017
$\text{MA}_3\text{Sb}_2\text{I}_9$	Solution/ Bulk crystal	40000	10^{12}	10	0.4 /0.9	[5]	2018
(TMHD)BiBr ₅	Solution/ Bulk crystal	100	N/A	10^3	8.9/10.2	[62]	2018
$\text{Cs}_2\text{AgBiBr}_6$	Solution/ Thin film	7010	5.66×10^{11}	10^4	0.956/0.995	[63]	2018
$\text{Cs}_2\text{SnCl}_{6-x}\text{Br}_x$	Solution/ Bulk crystal	N/A	2.71×10^{10}	N/A	N/A	[64]	2019
$\text{Cs}_3\text{Cu}_2\text{I}_5$	Solution/ Thin film	64.9	10^{11}	127	26.2/49.9	[65]	2019
(PEA) ₂ SnI ₄	Solution/ 2D	121	8.09×10^9	10^2	34/38	[66]	2019
$\text{Cs}_2\text{AgBiBr}_6$	Solution/ Thin film	1460	9.4×10^{12}	10^4	3.463/8.442	[67]	2019
$\text{Cs}_3\text{Sb}_2\text{Br}_9$	Solution/ Nanoflake	3800	2.6×10^{12}	N/A	48/24	[68]	2019
$\text{Cs}_3\text{Bi}_2\text{I}_9$	Solution/ Thin film	7.2	10^{11}	10^4	0.247/0.23	[69]	2020
Cs_2SnI_6	Solution/ Thin film	6	2×10^9	N/A	N/A	[70]	2020
$\text{AG}_3\text{Bi}_2\text{I}_9$	Thermal evaporation/ Bulk crystal	14.8	8.8×10^{10}	25	0.152/0.187	[71]	2020
$\text{Cs}_3\text{Sb}_2\text{I}_9$	CVD/ Nanoplate	40	1.26×10^{11}	10^4	0.096/0.058	This work	

Methods

Synthesis of $\text{Cs}_3\text{Sb}_2\text{I}_9$ Microplates: The $\text{Cs}_3\text{Sb}_2\text{I}_9$ microplates were grown in a single-zone horizontal tube furnace by a two-step CVD approach. Before the experiment, the sapphire or SiO_2 coated Si substrates were ultrasonically cleaned in acetone, ethanol, and deionized water for 15 minutes each at room temperature, respectively. The substrates were dried initially using a nitrogen drier and then on a hot plate at 60°C for 30 mins. In step-I, commercial CsI powder (99.9 %, metal basis, Sigma-Aldrich) was put in an alumina boat, which was placed at the center of the tube furnace heated up to 550°C with an optimized pressure of 2 Torr for a holding time of 10 minutes. High-purity argon (99.995 %) was used as the carrier gas at a flow rate of 200 sccm to transport the reactant vapor to the downstream of the quartz tube. The substrates were kept in the downstream side of the furnace. The distance between the source boat and substrate was 25 cm. In step-II, commercial SbI_3 powder (98 %, Sigma-Aldrich) was deposited at a controlled temperature of 130°C under 25 sccm of Ar flow, while the pressure and holding time remained the same as step-I. After each step, the furnace was cooled naturally under a continuous Ar flow. Prior to heating, the tube was evacuated to 5 mTorr with a mechanical pump. Next, Ar was injected into the tube for 30 mins for flushing to minimize oxygen and moisture before ramping up the temperature. The as-grown samples were then annealed at 180°C for 15 minutes inside the N_2 gas-filled tube furnace at atmospheric pressure to obtain $\text{Cs}_3\text{Sb}_2\text{I}_9$ perovskite microplates. The CsI and SbI_3 powders were used in a molar ratio of 1:3 to achieve a proper stoichiometric composition in these two steps. The growth process of $\text{Cs}_3\text{Sb}_2\text{I}_9$ mainly occurs at step-III (annealing process). It just contains melting and mixing of raw materials and recrystallizing of $\text{Cs}_3\text{Sb}_2\text{I}_9$, resulting in the final $\text{Cs}_3\text{Sb}_2\text{I}_9$ microplates, rather than epitaxial growth on the substrates. Therefore, the substrates have no significant impact on the growth results.

Fabrication of photodetectors: The substrates with prepared $\text{Cs}_3\text{Sb}_2\text{I}_9$ perovskite microplates were first fixed on a magnetic sample holder. Then, commercial Ni grids (Structure Probe, Inc., 300 mesh, with the square voids of $70\ \mu\text{m}$ side length) were aimed and put on the substrates under a optical microscope. Au electrodes, with the thickness of 40~50 nm, were next thermally evaporated onto the sample. After removing the Ni grids, square-shaped electrodes with $10\ \mu\text{m}$ apart were already formed on the microplates.

Characterization: XRD characterization was performed on a Bruker D2 system using $\text{Cu-K}\alpha$

radiation. High-resolution XRD and corresponding rocking curve were recorded by a Rigaku SmartLab X-ray diffractometer. The morphology and elemental composition of the sample were studied by a field-emission scanning electron microscope (FESEM, Philips XL30 FEG) equipped with energy-dispersive X-ray spectroscopy (EDX) capability. High-resolution transmission electron microscopy (HRTEM) image of the sample were obtained by a Tecnai G2 F20 S-TWIN microscope. Optical absorption measurements were conducted by a PerkinElmer Lambda 2S UV-vis spectrophotometer. Room temperature photoluminescence (PL) and mappings of $\text{Cs}_3\text{Sb}_2\text{I}_9$ microplates were performed by an WITec alpha300 R microscope with a 532 nm laser as the excitation source. Time-resolved PL spectra was obtained on an Edinburgh FLS 920 fluorescence spectrometer. The valence band spectrum was obtained by Ultraviolet-Ambient Pressure Photoemission Spectroscopy (UV-APS). Measurements were conducted using a KP technology (APS04) instrument in a N_2 -filled APS module. Hall mobility, conduction type and carrier density of material were recorded by a Hall effect measurement system (Ecopia HMS-5300). All the photodetector measurements were performed by using a standard probe station with an Agilent 4155C semiconductor analyzer coupled with lasers (261 nm, 405 nm, 450 nm, 532 nm, 650 nm) as the light source, whose power was measured by a Thorlabs PM400 power meter. The response times were evaluated by using an optical chopper (Sanford, SR540) to turn on and turn off the light that illuminated on the device. Also, a low noise current amplifier (Stanford, SR570) combined with a digital oscillator (Tektronix TBS 1102B EDU) were used to record the time and corresponding photocurrent values.

Acknowledgements

This work was supported by the National Natural Science Foundation of China under Grant No. 11874351, 11874352, 51672229 and 61805237, the Hong Kong Scholars Program (Grant No. XJ2019027), the General Research Fund (CityU 11204618) and the Theme-based Research (T42-103/16-N) of the Research Grants Council of Hong Kong SAR, China, CityU SGP-9380076 and the Foshan Innovative and Entrepreneurial Research Team Program (No. 2018IT100031).

Electronic Supplementary Material: Supplementary material (crystallographic data and 2D layered structure of the $\text{Cs}_3\text{Sb}_2\text{I}_9$ perovskite; SEM, AFM and EDX spectrum of $\text{Cs}_3\text{Sb}_2\text{I}_9$ microplates; Tauc plot of the absorption spectrum and 3D PL mapping of an individual microplate; TRPL spectrum of the microplates; the reproducible on/off switching of the

device under 0.5 V bias and at different temperatures from 80 K to 380 K; the reproducible on/off switching of the device measured after 100 days.) is available in the online version of this article at http://dx.doi.org/10.1007/s12274-***-****- (automatically inserted by the publisher).

References

- [1] Li, L.; Chen, H.; Fang, Z.; Meng, X.; Zuo, C.; Lv, M.; Tian, Y.; Fang, Y.; Xiao, Z.; Shan, C.; Xiao, Z.; Jin, Z.; Shen, G.; Shen, L.; Ding, L. An Electrically Modulated Single-Color/Dual-Color Imaging Photodetector. *Adv. Mater.* **2020**, *32*, 1907257.
- [2] Chen, H.; Liu, H.; Zhang, Z.; Hu, K.; Fang, X. Nanostructured Photodetectors: From Ultraviolet to Terahertz. *Adv. Mater.* **2016**, *28*, 403-433.
- [3] Xu, Y.; Lin, Q. Photodetectors based on solution-processable semiconductors: Recent advances and perspectives. *Appl. Phys. Rev.* **2020**, *7*, 011315.
- [4] Zhou, Q.; Park, J. G.; Nie, R.; Thokchom, A. K.; Ha, D.; Pan, J.; Seok, S. I.; Kim, T. Nanochannel-Assisted Perovskite Nanowires: From Growth Mechanisms to Photodetector Applications. *ACS Nano* **2018**, *12*, 8406-8414.
- [5] Yang, B.; Li, Y. J.; Tang, Y. X.; Mao, X.; Luo, C.; Wang, M. S.; Deng, W. Q.; Han, K. L. Constructing Sensitive and Fast Lead-Free Single-Crystalline Perovskite Photodetectors. *J. Phys. Chem. Lett.* **2018**, *9*, 3087-3092.
- [6] Hu, X.; Zhang, X.; Liang, L.; Bao, J.; Li, S.; Yang, W.; Xie, Y. High-Performance Flexible Broadband Photodetector Based on Organolead Halide Perovskite. *Adv. Funct. Mater.* **2014**, *24*, 7373-7380.
- [7] Dou, L.; Yang, Y. M.; You, J.; Hong, Z.; Chang, W. H.; Li, G.; Yang, Y. Solution-processed hybrid perovskite photodetectors with high detectivity. *Nat. Commun.* **2014**, *5*, 5404.
- [8] Liu, J.; Xue, Y.; Wang, Z.; Xu, Z. Q.; Zheng, C.; Weber, B.; Song, J.; Wang, Y.; Lu, Y.; Zhang, Y.; Bao, Q. Two-Dimensional CH₃NH₃PbI₃ Perovskite: Synthesis and Optoelectronic Application. *ACS Nano* **2016**, *10*, 3536-3542.
- [9] Dong Shi, V. A., Riccardo Comin, Mingjian Yuan, Erkki Alarousu, Andrei Buin, Yin Chen, Sjoerd Hoogland, Alexander Rothenberger, Khabiboulakh Katsiev, Yaroslav Losovyj, Xin Zhang, Peter A. Dowben, Omar F. Mohammed, Edward H. Sargent, Osman M. Bakr Low trap-state density and long carrier diffusion in organolead trihalide perovskite single crystals. *Science* **2015**, *347*, 519-522.
- [10] Wang, K.; Li, Z.; Zhou, F.; Wang, H.; Bian, H.; Zhang, H.; Wang, Q.; Jin, Z.; Ding, L.; Liu, S. Ruddlesden-Popper 2D Component to Stabilize γ -CsPbI₃ Perovskite Phase for Stable and Efficient Photovoltaics. *Adv. Energy Mater.* **2019**, *9*, 1902529.
- [11] Wang, H.; Bian, H.; Jin, Z.; Zhang, H.; Liang, L.; Wen, J.; Wang, Q.; Ding, L.; Liu, S. F. Cesium Lead Mixed-Halide Perovskites for Low-Energy Loss Solar Cells with Efficiency Beyond 17%. *Chem. Mater.* **2019**, *31*, 6231-6238.
- [12] Li, Z.; Zhou, F.; Wang, Q.; Ding, L.; Jin, Z. Approaches for thermodynamically stabilized CsPbI₃ solar cells. *Nano Energy* **2020**, *71*, 104634.
- [13] Bian, H.; Wang, H.; Li, Z.; Zhou, F.; Xu, Y.; Zhang, H.; Wang, Q.; Ding, L.; Liu, S. F.; Jin, Z. Unveiling the Effects of Hydrolysis-Derived DMAI/DMAPI x Intermediate Compound on the Performance of CsPbI₃ Solar Cells. *Adv. Sci.* **2020**, *7*, 1902868.
- [14] Wang, F.; Mei, J.; Wang, Y.; Zhang, L.; Zhao, H.; Zhao, D. Fast Photoconductive Responses in Organometal Halide Perovskite Photodetectors. *ACS Appl. Mater. Interfaces* **2016**, *8*, 2840-2846.
- [15] Juarez-Perez, E. J.; Hawash, Z.; Raga, S. R.; Ono, L. K.; Qi, Y. Thermal degradation of CH₃NH₃PbI₃ perovskite into NH₃ and CH₃I gases observed by coupled thermogravimetry-mass spectrometry analysis. *Energy Environ. Sci.* **2016**, *9*, 3406-3410.
- [16] Conings, B.; Drijkoningen, J.; Gauquelin, N.; Babayigit, A.; D'Haen, J.; D'Olieslaeger, L.; Ethirajan, A.; Verbeeck, J.; Manca, J.; Mosconi, E.; Angelis, F. D.; Boyen, H.-G. Intrinsic Thermal Instability of Methylammonium Lead Trihalide Perovskite. *Adv. Energy Mater.* **2015**, *5*, 1500477.
- [17] Jinli Yang, B. D. S., Dianyi Liu, Timothy L. Kelly Investigation of CH₃NH₃PbI₃ Degradation Rates and Mechanisms in Controlled Humidity Environments Using in Situ Techniques. *ACS Nano* **2015**, *9*, 1955-1963.
- [18] De Roo, J.; Ibanez, M.; Geiregat, P.; Nedelcu, G.; Walravens, W.; Maes, J.; Martins, J. C.; Van Driessche, I.; Kovalenko, M. V.; Hens, Z. Highly Dynamic Ligand Binding and Light Absorption Coefficient of Cesium Lead Bromide Perovskite Nanocrystals. *ACS Nano* **2016**, *10*, 2071-2081.
- [19] Akkerman, Q. A.; D'Innocenzo, V.; Accornero, S.; Scarpellini, A.; Petrozza, A.; Prato, M.; Manna, L. Tuning the Optical Properties of Cesium Lead Halide Perovskite Nanocrystals by Anion Exchange Reactions. *J. Am. Chem. Soc.* **2015**, *137*, 10276-10281.
- [20] Yettapu, G. R.; Talukdar, D.; Sarkar, S.; Swarnkar, A.; Nag, A.; Ghosh, P.; Mandal, P. Terahertz Conductivity within Colloidal CsPbBr₃ Perovskite Nanocrystals: Remarkably High Carrier Mobilities and Large Diffusion Lengths. *Nano Lett.* **2016**, *16*, 4838-4848.
- [21] Sun, S.; Yuan, D.; Xu, Y.; Wang, A.; Deng, Z. Ligand-Mediated Synthesis of Shape-Controlled Cesium Lead Halide Perovskite Nanocrystals via Reprecipitation Process at Room Temperature. *ACS Nano* **2016**, *10*, 3648-3657.
- [22] Pradhan, B.; Kumar, G. S.; Sain, S.; Dalui, A.; Ghorai, U. K.; Pradhan, S. K.; Acharya, S. Size Tunable

- Cesium Antimony Chloride Perovskite Nanowires and Nanorods. *Chem. Mater.* **2018**, *30*, 2135-2142.
- [23] Tong, X. W.; Kong, W. Y.; Wang, Y. Y.; Zhu, J. M.; Luo, L. B.; Wang, Z. H. High-Performance Red-Light Photodetector Based on Lead-Free Bismuth Halide Perovskite Film. *ACS Appl. Mater. Interfaces* **2017**, *9*, 18977-18985.
- [24] Chen, J.; Luo, Z.; Fu, Y.; Wang, X.; Czech, K. J.; Shen, S.; Guo, L.; Wright, J. C.; Pan, A.; Jin, S. Tin(IV)-Tolerant Vapor-Phase Growth and Photophysical Properties of Aligned Cesium Tin Halide Perovskite (CsSnX_3 ; X = Br, I) Nanowires. *ACS Energy Lett.* **2019**, *4*, 1045-1052.
- [25] Huang, H.; Bodnarchuk, M. I.; Kershaw, S. V.; Kovalenko, M. V.; Rogach, A. L. Lead Halide Perovskite Nanocrystals in the Research Spotlight: Stability and Defect Tolerance. *ACS Energy Lett.* **2017**, *2*, 2071-2083.
- [26] Hoefler, S. F.; Trimmel, G.; Rath, T. Progress on lead-free metal halide perovskites for photovoltaic applications: a review. *Monatsh. Chem.* **2017**, *148*, 795-826.
- [27] Parrott, E. S.; Milot, R. L.; Stergiopoulos, T.; Snaith, H. J.; Johnston, M. B.; Herz, L. M. Effect of Structural Phase Transition on Charge-Carrier Lifetimes and Defects in $\text{CH}_3\text{NH}_3\text{SnI}_3$ Perovskite. *J. Phys. Chem. Lett.* **2016**, *7*, 1321-1326.
- [28] Hao, F.; Stoumpos, C. C.; Cao, D. H.; Chang, R. P. H.; Kanatzidis, M. G. Lead-free solid-state organic-inorganic halide perovskite solar cells. *Nat. Photonics* **2014**, *8*, 489-494.
- [29] Noel, N. K.; Stranks, S. D.; Abate, A.; Wehrenfennig, C.; Guarnera, S.; Haghighirad, A.-A.; Sadhanala, A.; Eperon, G. E.; Pathak, S. K.; Johnston, M. B.; Petrozza, A.; Herz, L. M.; Snaith, H. J. Lead-free organic-inorganic tin halide perovskites for photovoltaic applications. *Energy Environ. Sci.* **2014**, *7*, 3061-3068.
- [30] Hebig, J.-C.; Kühn, I.; Flohre, J.; Kirchartz, T. Optoelectronic Properties of $(\text{CH}_3\text{NH}_3)_3\text{Sb}_2\text{I}_9$ Thin Films for Photovoltaic Applications. *ACS Energy Lett.* **2016**, *1*, 309-314.
- [31] Chatterjee, S.; Pal, A. J. Tin(IV) Substitution in $(\text{CH}_3\text{NH}_3)_3\text{Sb}_2\text{I}_9$: Toward Low-Band-Gap Defect-Ordered Hybrid Perovskite Solar Cells. *ACS Appl. Mater. Interfaces* **2018**, *10*, 35194-35205.
- [32] Umar, F.; Zhang, J.; Jin, Z.; Muhammad, I.; Yang, X.; Deng, H.; Jahangeer, K.; Hu, Q.; Song, H.; Tang, J. Dimensionality Controlling of $\text{Cs}_3\text{Sb}_2\text{I}_9$ for Efficient All-Inorganic Planar Thin Film Solar Cells by HCl-Assisted Solution Method. *Adv. Optical Mater.* **2019**, *7*, 1801368.
- [33] Zuo, C.; Ding, L. Lead-free Perovskite Materials $(\text{NH}_4)_3\text{Sb}_2\text{I}_x\text{Br}_{9-x}$. *Angew. Chem. Int. Ed.* **2017**, *56*, 6528-6532.
- [34] Ma, Z.; Shi, Z.; Yang, D.; Zhang, F.; Li, S.; Wang, L.; Wu, D.; Zhang, Y.; Na, G.; Zhang, L.; Li, X.; Zhang, Y.; Shan, C. Electrically-Driven Violet Light-Emitting Devices Based on Highly Stable Lead-Free Perovskite $\text{Cs}_3\text{Sb}_2\text{Br}_9$ Quantum Dots. *ACS Energy Lett.* **2020**, *5*, 385-394.
- [35] Zhang, J.; Yang, Y.; Deng, H.; Farooq, U.; Yang, X.; Khan, J.; Tang, J.; Song, H. High Quantum Yield Blue Emission from Lead-Free Inorganic Antimony Halide Perovskite Colloidal Quantum Dots. *ACS Nano* **2017**, *11*, 9294-9302.
- [36] Singh, A.; Boopathi, K. M.; Mohapatra, A.; Chen, Y. F.; Li, G.; Chu, C. W. Photovoltaic Performance of Vapor-Assisted Solution-Processed Layer Polymorph of $\text{Cs}_3\text{Sb}_2\text{I}_9$. *ACS Appl. Mater. Interfaces* **2018**, *10*, 2566-2573.
- [37] Correa-Baena, J.-P.; Nienhaus, L.; Kurchin, R. C.; Shin, S. S.; Wieghold, S.; Putri Hartono, N. T.; Layurova, M.; Klein, N. D.; Poindexter, J. R.; Polizzotti, A.; Sun, S.; Bawendi, M. G.; Buonassisi, T. A-Site Cation in Inorganic $\text{A}_3\text{Sb}_2\text{I}_9$ Perovskite Influences Structural Dimensionality, Exciton Binding Energy, and Solar Cell Performance. *Chem. Mater.* **2018**, *30*, 3734-3742.
- [38] Park, B. W.; Philippe, B.; Zhang, X.; Rensmo, H.; Boschloo, G.; Johansson, E. M. Bismuth Based Hybrid Perovskites $\text{A}_3\text{Bi}_2\text{I}_9$ (A: Methylammonium or Cesium) for Solar Cell Application. *Adv. Mater.* **2015**, *27*, 6806-6813.
- [39] Li, J.; Luo, L.; Huang, H.; Ma, C.; Ye, Z.; Zeng, J.; He, H. 2D Behaviors of Excitons in Cesium Lead Halide Perovskite Nanoplatelets. *J Phys Chem Lett* **2017**, *8*, 1161-1168.
- [40] Yang, Z.; Wang, M.; Qiu, H.; Yao, X.; Lao, X.; Xu, S.; Lin, Z.; Sun, L.; Shao, J. Engineering the Exciton Dissociation in Quantum-Confined 2D CsPbBr_3 Nanosheet Films. *Adv. Funct. Mater.* **2018**, *28*, 1705908.
- [41] Jain, S. M.; Phuyal, D.; Davies, M. L.; Li, M.; Philippe, B.; De Castro, C.; Qiu, Z.; Kim, J.; Watson, T.; Tsoi, W. C.; Karis, O.; Rensmo, H.; Boschloo, G.; Edvinsson, T.; Durrant, J. R. An effective approach of vapour assisted morphological tailoring for reducing metal defect sites in lead-free, $(\text{CH}_3\text{NH}_3)_3\text{Bi}_2\text{I}_9$ bismuth-based perovskite solar cells for improved performance and long-term stability. *Nano Energy* **2018**, *49*, 614-624.
- [42] Yang, B.; Yin, L.; Niu, G.; Yuan, J. H.; Xue, K. H.; Tan, Z.; Miao, X. S.; Niu, M.; Du, X.; Song, H.; Lifshitz, E.; Tang, J. Lead-Free Halide Rb_2CuBr_3 as Sensitive X-Ray Scintillator. *Adv. Mater.* **2019**, *31*, 1904711.
- [43] Liu, M.; Zhong, G.; Yin, Y.; Miao, J.; Li, K.; Wang, C.; Xu, X.; Shen, C.; Meng, H. Aluminum-Doped Cesium Lead Bromide Perovskite Nanocrystals with Stable Blue Photoluminescence Used for Display Backlight. *Adv. Sci.* **2017**, *4*, 1700335.
- [44] Swarnkar, A.; Chulliyil, R.; Ravi, V. K.; Irfanullah, M.; Chowdhury, A.; Nag, A. Colloidal CsPbBr_3 Perovskite Nanocrystals: Luminescence beyond Traditional Quantum Dots. *Angew. Chem. Int. Ed.* **2015**, *54*, 15424-15428.
- [45] Jun, T.; Sim, K.; Iimura, S.; Sasase, M.; Kamioka, H.; Kim, J.; Hosono, H. Lead-Free Highly Efficient

- Blue-Emitting $\text{Cs}_3\text{Cu}_2\text{I}_5$ with 0D Electronic Structure. *Adv. Mater.* **2018**, *30*, 1804547.
- [46] Lian, L.;Zheng, M.;Zhang, W.;Yin, L.;Du, X.;Zhang, P.;Zhang, X.;Gao, J.;Zhang, D.;Gao, L.;Niu, G.;Song, H.;Chen, R.;Lan, X.;Tang, J.; Zhang, J. Efficient and Reabsorption-Free Radioluminescence in $\text{Cs}_3\text{Cu}_2\text{I}_5$ Nanocrystals with Self-Trapped Excitons. *Adv. Sci.* **2020**, *7*, 2000195.
- [47] Ma, Z.;Shi, Z.;Qin, C.;Cui, M.;Yang, D.;Wang, X.;Wang, L.;Ji, X.;Chen, X.;Sun, J.;Wu, D.;Zhang, Y.;Li, X. J.;Zhang, L.; Shan, C. Stable Yellow Light-Emitting Devices Based on Ternary Copper Halides with Broadband Emissive Self-Trapped Excitons. *ACS Nano* **2020**, *14*, 4475-4486.
- [48] Li, Y.;Shi, Z.;Wang, L.;Chen, Y.;Liang, W.;Wu, D.;Li, X.;Zhang, Y.;Shan, C.; Fang, X. Solution-processed one-dimensional CsCu_2I_3 nanowires for polarization-sensitive and flexible ultraviolet photodetectors. *Mater. Horizons* **2020**, *7*, 1613-1622.
- [49] Xie, B.;Xie, R.;Zhang, K.;Yin, Q.;Hu, Z.;Yu, G.;Huang, F.; Cao, Y. Self-filtering narrowband high performance organic photodetectors enabled by manipulating localized Frenkel exciton dissociation. *Nat. Commun.* **2020**, *11*, 2871.
- [50] Gong, Y.;Liu, Q.;Gong, M.;Wang, T.;Zeng, G.;Chan, W.-L.; Wu, J. High-Performance Photodetectors Based on Effective Exciton Dissociation in Protein-Adsorbed Multiwalled Carbon Nanotube Nanohybrids. *Adv. Optical Mater.* **2017**, *5*, 1600478.
- [51] McCall, K. M.;Stoumpos, C. C.;Kostina, S. S.;Kanatidis, M. G.; Wessels, B. W. Strong Electron-Phonon Coupling and Self-Trapped Excitons in the Defect Halide Perovskites $\text{A}_3\text{M}_2\text{I}_9$ (A = Cs, Rb; M = Bi, Sb). *Chem. Mater.* **2017**, *29*, 4129-4145.
- [52] Toyozawa, Y. Further Contribution to the Theory of the Line-Shape of the Exciton Absorption Band. *Prog. Theor. Phys.* **1962**, *27*, 89-104.
- [53] K. R. Dawson, D. P. F Band Absorption in Alkali Halides as a Function of Temperature. *Phys. Status Solidi B* **1969**, *35*, 95-105.
- [54] C. H. Leung, K. S. S. On the luminescence quenching of F centres in alkali halides. *Solid State Commun.* **1980**, *33*, 907-910.
- [55] Franz. Urbach The long-wavelength edge of photographic sensitivity and electronic absorption of solids. *Phys. Rev.* **1953**, *92*, 1324.
- [56] Masada, S.;Yamada, T.;Tahara, H.;Hirori, H.;Saruyama, M.;Kawawaki, T.;Sato, R.;Teranishi, T.; Kanemitsu, Y. Effect of A-Site Cation on Photoluminescence Spectra of Single Lead Bromide Perovskite Nanocrystals. *Nano Lett.* **2020**, *20*, 4022-4028.
- [57] van Roosbroeck, W.; Shockley, W. Photon-Radiative Recombination of Electrons and Holes in Germanium. *Phys. Rev.* **1954**, *94*, 1558-1560.
- [58] Olson, C. G.; Lynch, D. W. Longitudinal-Optical-Phonon-Plasmon Coupling in GaAs. *Phys. Rev.* **1969**, *177*, 1231-1234.
- [59] Konstantatos, G.; Clifford, J.; Levina, L.; Sargent, E. H. Sensitive solution-processed visible-wavelength photodetectors. *Nat. Photon.* **2007**, *1*, 531-534
- [60] Liu, Y.; Zhang, Y.; Yang, Z.; Ye, H.; Feng, J.; Xu, Z.; Zhang, X.; Munir, R.; Liu, J.; Zuo, P.; Li, Q.; Hu, M.; Meng, L.; Wang, K.; Smilgies, D. M.; Zhao, G.; Xu, H.; Yang, Z.; Amassian, A.; Li, J.; Zhao, K.; Liu, F. S. Multi-inch single-crystalline perovskite membrane for high-detectivity flexible photosensors. *Nat. Commun.* **2018**, *9*, 5302.
- [61] Waleed, A.;Tavakoli, M. M.;Gu, L.;Wang, Z.;Zhang, D.;Manikandan, A.;Zhang, Q.;Zhang, R.;Chueh, Y. L.; Fan, Z. Lead-Free Perovskite Nanowire Array Photodetectors with Drastically Improved Stability in Nanoengineering Templates. *Nano Lett.* **2017**, *17*, 523-530.
- [62] Ji, C.;Wang, P.;Wu, Z.;Sun, Z.;Li, L.;Zhang, J.;Hu, W.;Hong, M.; Luo, J. Inch-Size Single Crystal of a Lead-Free Organic-Inorganic Hybrid Perovskite for High-Performance Photodetector. *Adv. Funct. Mater.* **2018**, *28*, 1705467.
- [63] Lei, L.-Z.;Shi, Z.-F.;Li, Y.;Ma, Z.-Z.;Zhang, F.;Xu, T.-T.;Tian, Y.-T.;Wu, D.;Li, X.-J.; Du, G.-T. High-efficiency and air-stable photodetectors based on lead-free double perovskite $\text{Cs}_2\text{AgBiBr}_6$ thin films. *J. Mater. Chem. C* **2018**, *6*, 7982-7988.
- [64] Zhou, J.;Luo, J.;Rong, X.;Wei, P.;Molokeev, M. S.;Huang, Y.;Zhao, J.;Liu, Q.;Zhang, X.;Tang, J.; Xia, Z. Lead-Free Perovskite Derivative Single Crystals for Narrowband Photodetectors. *Adv. Optical Mater.* **2019**, *7*, 1900139.
- [65] Zhang, Z. X.;Li, C.;Lu, Y.;Tong, X. W.;Liang, F. X.;Zhao, X. Y.;Wu, D.;Xie, C.; Luo, L. B. Sensitive Deep Ultraviolet Photodetector and Image Sensor Composed of Inorganic Lead-Free $\text{Cs}_3\text{Cu}_2\text{I}_5$ Perovskite with Wide Bandgap. *J. Phys. Chem. Lett.* **2019**, *10*, 5343-5350.
- [66] Fang, C.;Wang, H.;Shen, Z.;Shen, H.;Wang, S.;Ma, J.;Wang, J.;Luo, H.; Li, D. High-Performance Photodetectors Based on Lead-Free 2D Ruddlesden-Popper Perovskite/ MoS_2 Heterostructures. *ACS Appl. Mater. Interfaces* **2019**, *11*, 8419-8427.
- [67] Li, Y.;Shi, Z.;Lei, L.;Li, S.;Yang, D.;Wu, D.;Xu, T.;Tian, Y.;Lu, Y.;Wang, Y.;Zhang, L.;Li, X.;Zhang, Y.;Du, G.; Shan, C. Ultrastable Lead-Free Double Perovskite Photodetectors with Imaging Capability. *Advanced Materials Interfaces* **2019**, *6*, 1900188.
- [68] Zheng, Z.;Hu, Q.;Zhou, H.;Luo, P.;Nie, A.;Zhu, H.;Gan, L.;Zhuge, F.;Ma, Y.;Song, H.; Zhai, T. Submillimeter and lead-free $\text{Cs}_3\text{Sb}_2\text{Br}_9$ perovskite nanoflakes: inverse temperature crystallization growth and application for ultrasensitive photodetectors. *Nanoscale Horiz.* **2019**, *4*, 1372-1379.

- [69] Li, W. G.; Wang, X. D.; Liao, J. F.; Jiang, Y.; Kuang, D. B. Enhanced On–Off Ratio Photodetectors Based on Lead-Free Single Crystal Thin Films. *Adv. Funct. Mater.* **2020**, *30*, 1909701.
- [70] Krishnaiah, M.; Khan, M. M. I.; Kumar, A.; Jin, S. H. Impact of CsI concentration, relative humidity, and annealing temperature on lead-free Cs_2SnI_6 perovskites: Toward visible light photodetectors application. *Mater. Lett.* **2020**, *269*, 127675.
- [71] Zhang, W.; Sui, Y.; Kou, B.; Peng, Y.; Wu, Z.; Luo, J. Large-Area Exfoliated Lead-Free Perovskite-Derivative Single-Crystalline Membrane for Flexible Low-Defect Photodetectors. *ACS Appl. Mater. Interfaces* **2020**, *12*, 9141-9149.
- [72] Tian, C.; Wang, F.; Wang, Y.; Yang, Z.; Chen, X.; Mei, J.; Liu, H.; Zhao, D. Chemical Vapor Deposition Method Grown All-Inorganic Perovskite Microcrystals for Self-Powered Photodetectors. *ACS Appl. Mater. Interfaces* **2019**, *11*, 15804-15812.

Electronic Supplementary Material

Crystalline All-Inorganic Lead-Free Cs₃Sb₂I₉ Perovskite Microplates with Ultra-Fast Photoconductive Response and Robust Thermal Stability

Sujit Kumer Shil,^{1,3,§} Fei Wang,^{2,4,5,§} (✉) Zhengxun Lai,² You Meng,² Yunpeng Wang,⁴ Dongxu Zhao,⁴ Mohammad Kamal Hossain,^{1,6} Kingsley O. Egbo,¹ Ying Wang,¹ Kin Man Yu,¹ (✉) and Johnny C. Ho^{2,5} (✉)

¹ Department of Physics, City University of Hong Kong, Kowloon, Hong Kong SAR

² Department of Materials Science and Engineering, City University of Hong Kong, Kowloon, Hong Kong SAR

³ Department of Physics, Khulna University of Engineering & Technology (KUET), Khulna, Bangladesh

⁴ State Key Laboratory of Luminescence and Applications, Changchun Institute of Optics, Fine Mechanics and Physics, Chinese Academy of Sciences, 3888 Dongnanhu Road, Changchun 130021, China

⁵ State Key Laboratory of Terahertz and Millimeter Waves, City University of Hong Kong, Kowloon, Hong Kong SAR

⁶ Department of Physics, Comilla University, Kotbari, Comilla 3506, Bangladesh

[§] Sujit Kumer Shil and Fei Wang contributed equally to this work.

Supporting information to DOI 10.1007/s12274-****-****-* (automatically inserted by the publisher)

Table S1: Crystallographic data for Cs₃Sb₂I₉ perovskite¹

Compound	Cs ₃ Sb ₂ I ₉			
Lattice parameters	a= b= 8.687Å, c= 10.603Å $\alpha=\beta=90^\circ$, $\gamma=120^\circ$			
Volume	693.004Å ³			
Density	4.28g/cm ³			
Space group	P $\bar{3}$ m1			
Crystal system	Trigonal			
Fractional co-ordinates	atom	a	b	c
	Cs	0	0	0
		0.3333	0.6667	0.3257
		0.6667	0.3333	0.6743
	Sb	0.3333	0.6667	0.8154
		0.6667	0.3333	0.1846
	I	0	0.5	0
		0.1714	0.8286	0.6644
		0.1714	0.3428	0.6644
		0.3428	0.1714	0.3356
		0.5	0.5	0
		0.5	0	0
		0.6572	0.8286	0.6644
		0.8286	0.6572	0.3356
		0.8286	0.1714	0.3356

[1] Persson Kristin, “Materials Data on Cs₃Sb₂I₉ (SG: 164) by Materials Project”, 2014, United States, doi 10.17188/1264913.

Schematic illustration of the two-step chemical vapor deposition

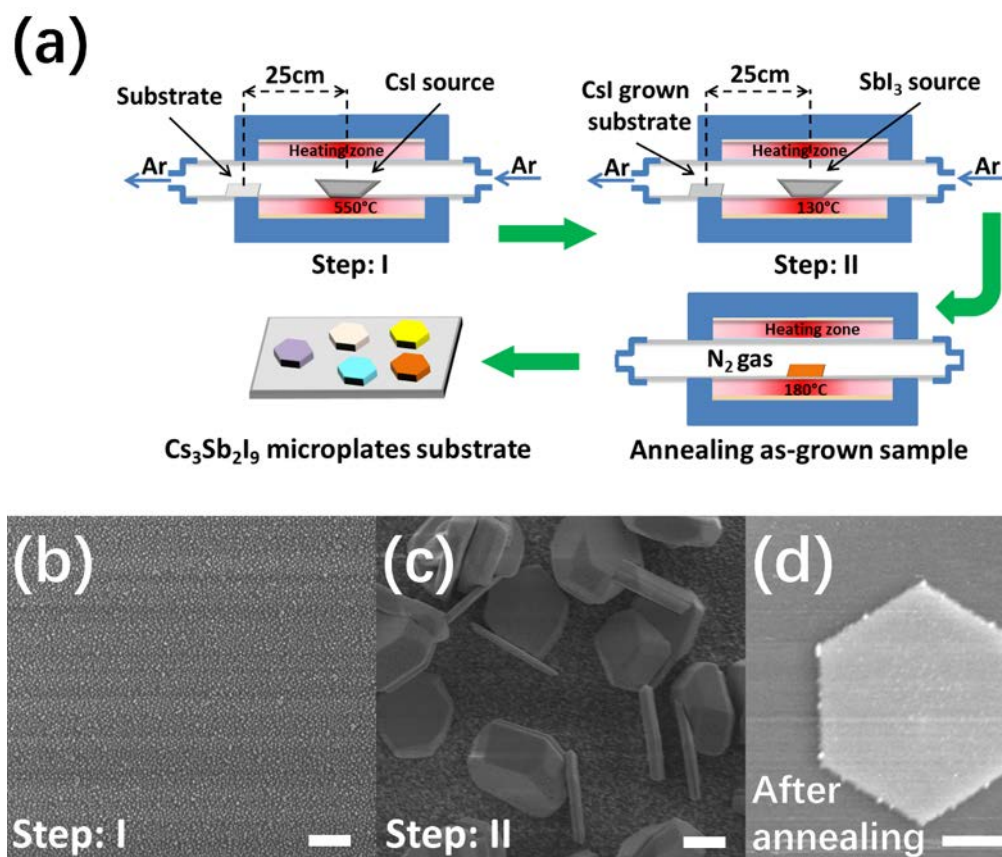


Figure S1. (a) Schematic illustration of the two-step chemical vapor deposition of Cs₃Sb₂I₉ perovskite microplates. (b), (c) and (d) SEM images of the sample obtained after each growth step, demonstrating the microplate evolution. Scale bars on the SEM images are 10 μ m.

SEM image of CVD grown SbI_3 microplates

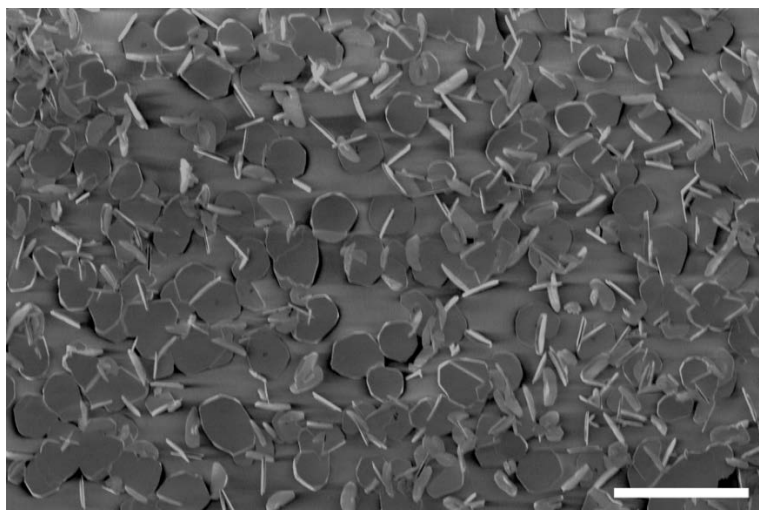


Figure S2. A SEM image of CVD grown SbI_3 on the sapphire substrate. The scale bar is 50 μm .

Schematic representation of the crystal structure

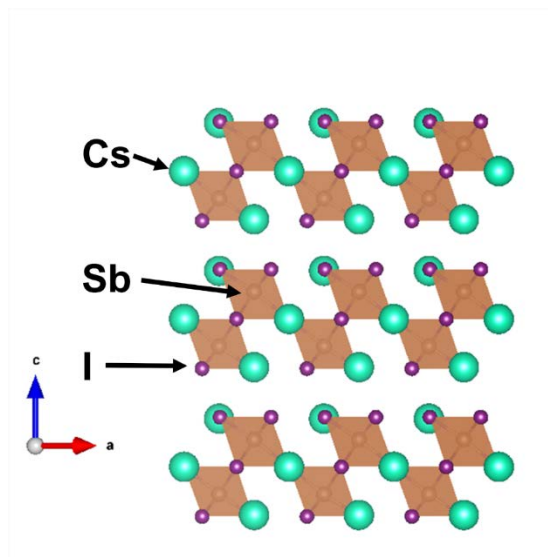


Figure S3. A schematic representation of the crystal structure of 2D layered $\text{Cs}_3\text{Sb}_2\text{I}_9$ perovskite. Green, brown, and violet colored spheres represent Cs, Sb, and I, respectively.

XRD patterns of CVD grown CsI and SbI₃

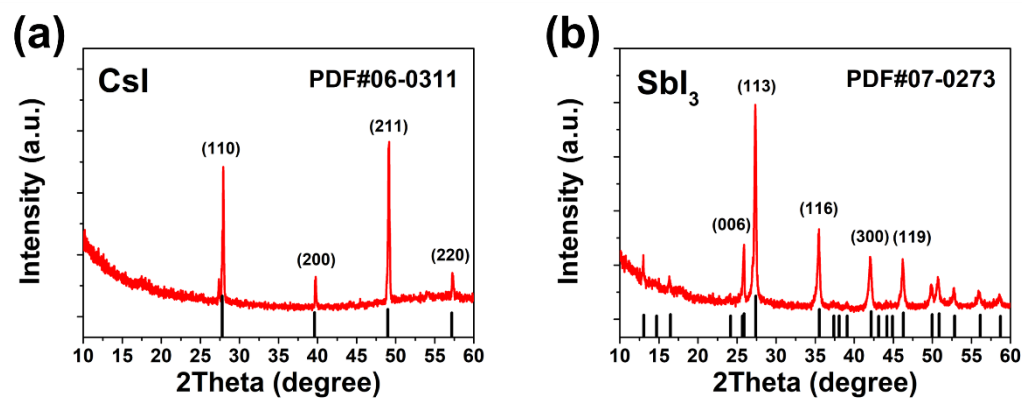


Figure S4. XRD patterns of CVD grown CsI (c) and SbI₃ (d).

Thickness of $\text{Cs}_3\text{Sb}_2\text{I}_9$ perovskite microplates

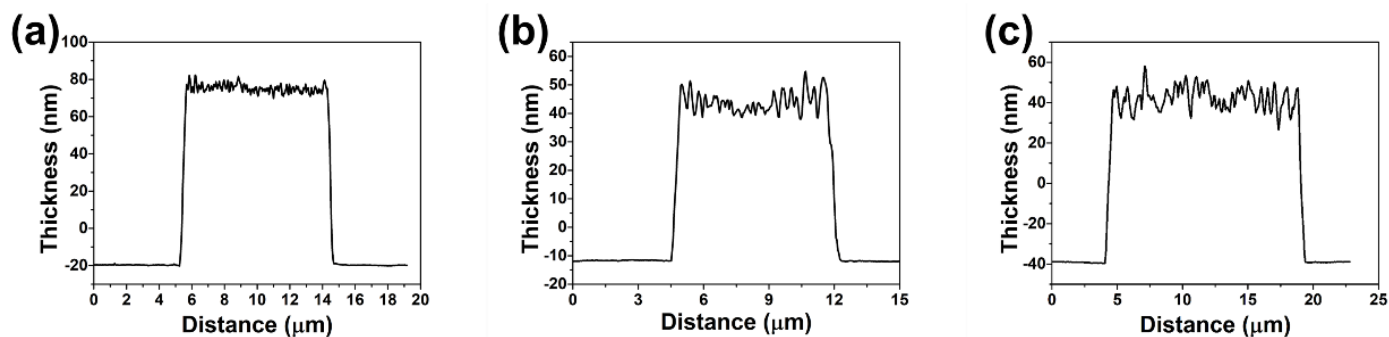


Figure S5. AFM line profile results showing the thickness of $\text{Cs}_3\text{Sb}_2\text{I}_9$ perovskite microplates.

EDX spectrum of a $\text{Cs}_3\text{Sb}_2\text{I}_9$ perovskite microplates

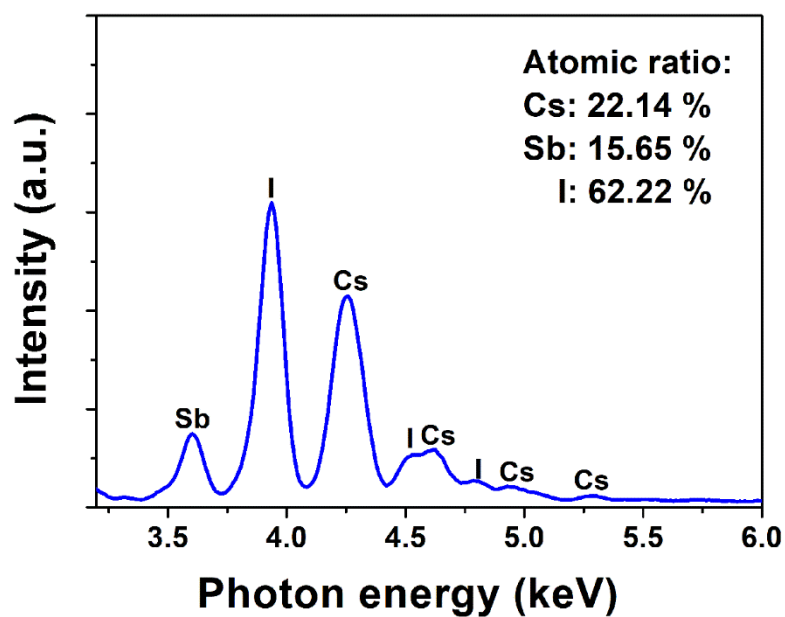


Figure S6. EDX spectrum of a $\text{Cs}_3\text{Sb}_2\text{I}_9$ perovskite microplates showing the presence of the different component elements and their elemental composition.

EDX mapping of a $\text{Cs}_3\text{Sb}_2\text{I}_9$ perovskite microplate

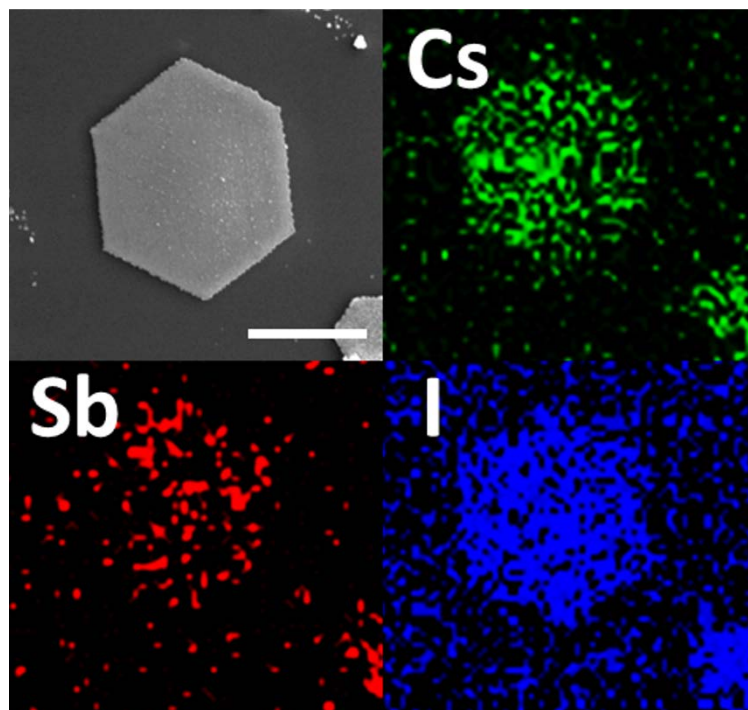


Figure S7. EDX mapping of a typical $\text{Cs}_3\text{Sb}_2\text{I}_9$ perovskite microplate.

Tauc plot of the absorption spectrum

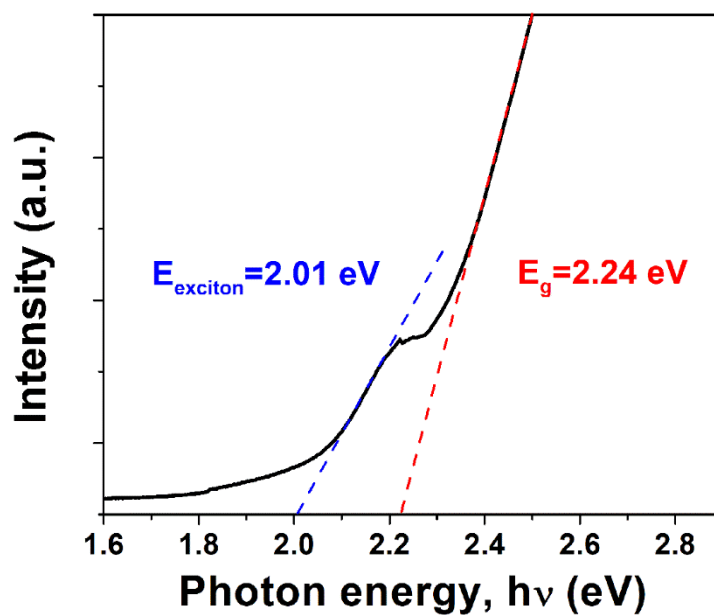


Figure S8. A Tauc plot of the absorption spectrum showing the bandgap energy and exciton edge of Cs₃Sb₂I₉ microplates.

Quantum-well absorption model fitting

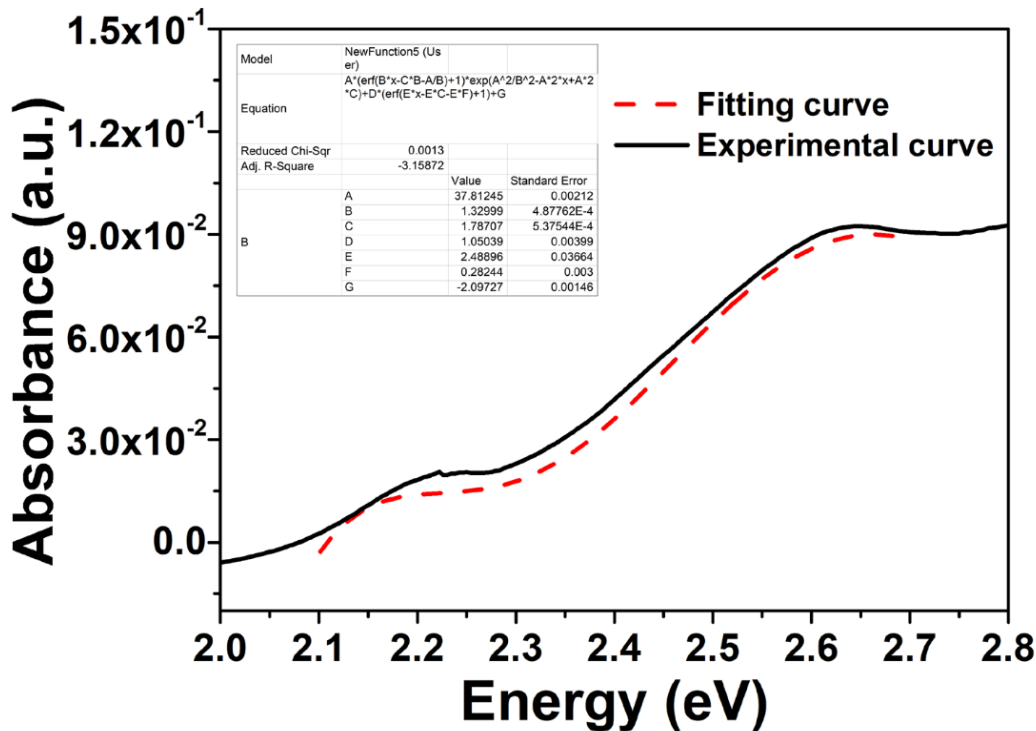


Figure S9. Experimental absorbance and the best fit spectra using the quantum-well absorption model.

The quantum-well absorption model can be described with the following analytical expressions:

$$p(E) = p_x + \frac{A_C}{2} \left[\text{erf} \left(\frac{(E - E_0) - E_b^x}{\gamma_C} \right) + 1 \right] \quad (1)$$

$$p_x = \frac{1}{2\eta} \left[\text{erf} \left(\frac{(E - E_0)}{\gamma_C} - \frac{\gamma}{2\eta} \right) + 1 \right] \exp \left(\frac{\gamma^2}{4\eta^2} - \frac{E - E_0}{\eta} \right) \quad (2)$$

where p_x is the absorption line shape for a quantum-well exciton with asymmetric broadening η . E_0 and E_b^x are the absolute exciton energy and binding energy, respectively. γ is the line width of the absorption peak. A_C and γ_C are the step height and width of the continuum edge.

PL mapping of a typical $\text{Cs}_3\text{Sb}_2\text{I}_9$ microplate

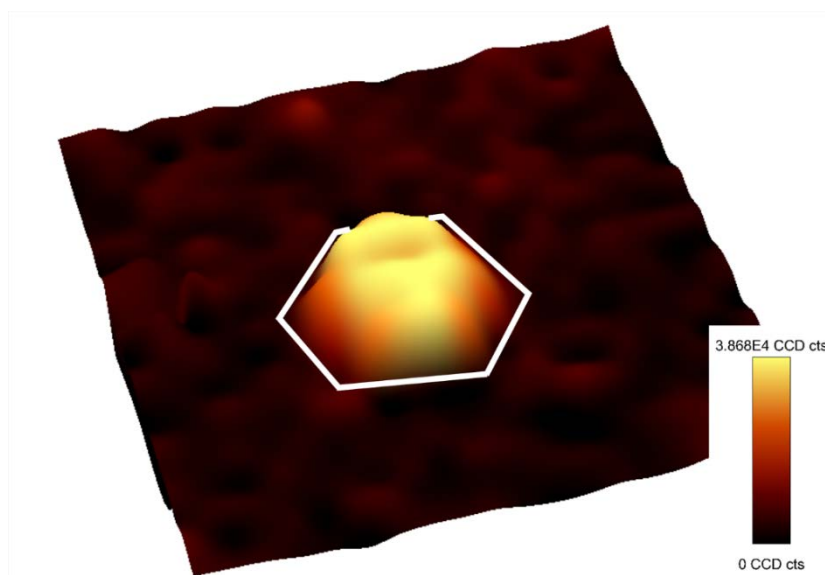


Figure S10. Three-dimensional PL mapping of a typical $\text{Cs}_3\text{Sb}_2\text{I}_9$ microplate.

PL lifetime

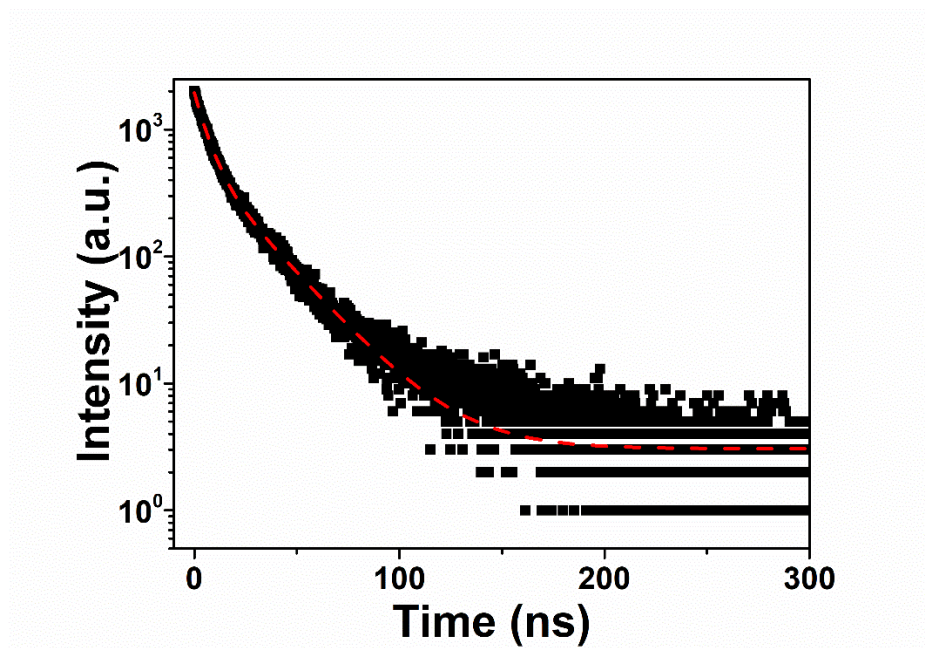


Figure S11. Time-resolved PL spectrum of the $\text{Cs}_3\text{Sb}_2\text{I}_9$ microplates.

The measured PL lifetime can be obtained by fitting the PL decay curve with a biexponential formula:

$$f(t) = A + B_1 \exp\left(-\frac{t}{\tau_1}\right) + B_2 \exp\left(-\frac{t}{\tau_2}\right) \quad (3)$$

where A , B_1 (B_2), and τ_1 (τ_2) are constant, decay amplitudes and decay times, respectively.

The reproducible on/off switching of the device

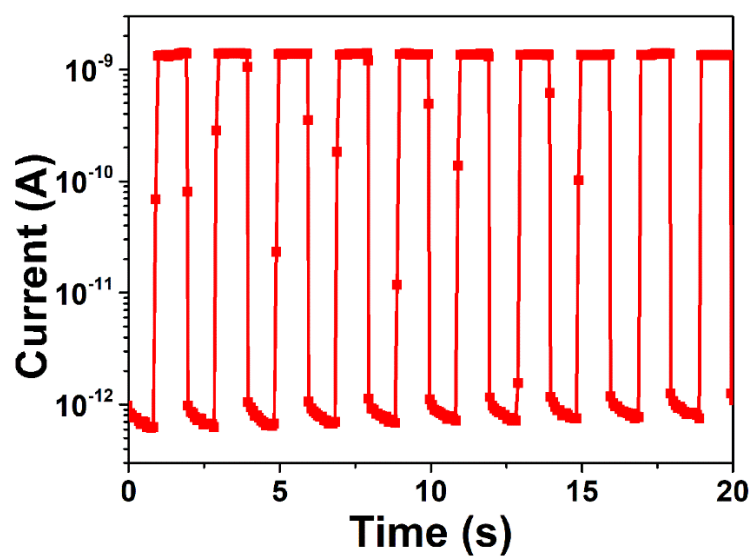


Figure S12. The reproducible on/off switching of the device under 0.5 V bias upon 532 nm light illumination with a power density of 47 mW/cm².

The reproducible on/off switching of the device measured at different temperatures

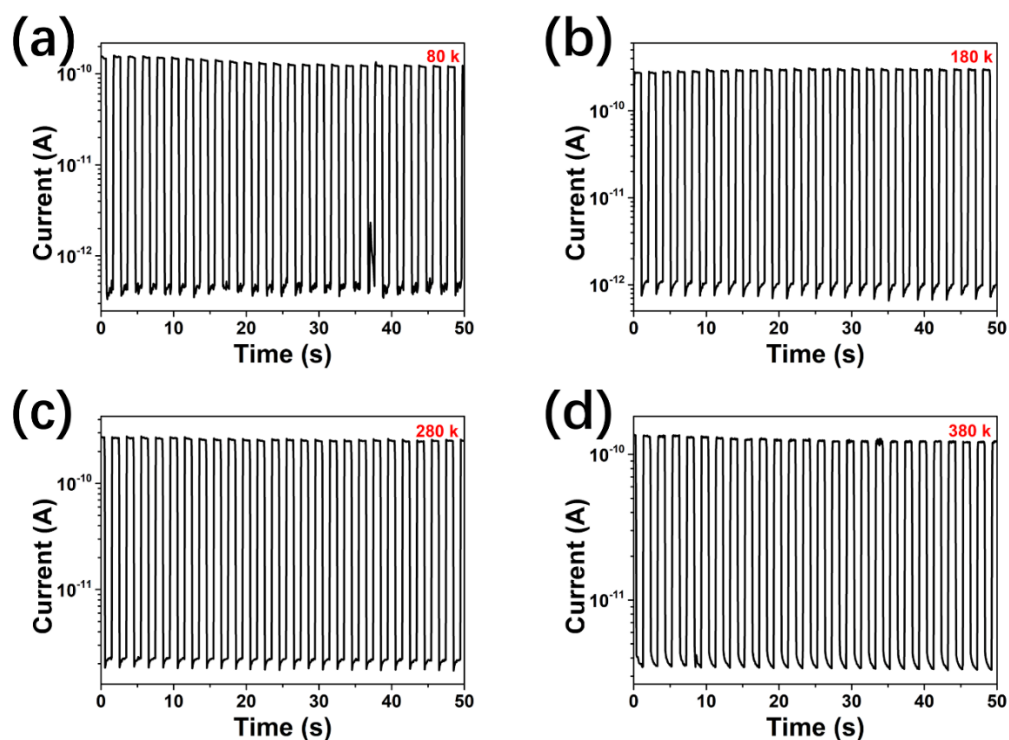


Figure S13. The reproducible on/off switching of the device measured at different temperatures with the bias voltage of 1 V (20 mW/cm^2 at 532 nm irradiation wavelength).

Long-term stability of the device

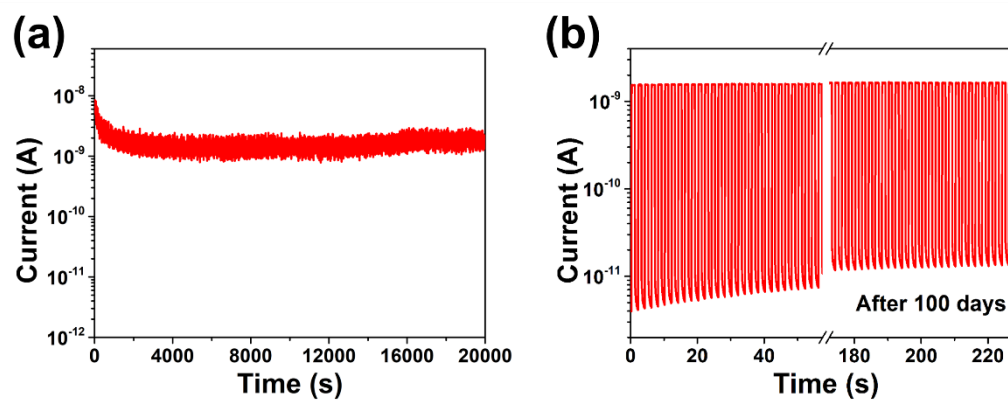


Figure S14. (a) The photocurrent stability of the device. (b) The reproducible on/off switching of the device measured after 100 days.

Address correspondence to Fei Wang, wangf@ciomp.ac.cn; Kin Man Yu, kinmanyu@cityu.edu.hk; Johnny C. Ho, johnnyho@cityu.edu.hk